QUANTUM MODELING OF DARK MATTER IN GALACTIC HALOS

by

SHANE CHARLES SPIVEY

Presented to the Faculty of the Graduate School of
The University of Texas at Arlington in Partial Fulfillment
of the Requirements
for the Degree of

DOCTOR OF PHILOSOPHY

THE UNIVERSITY OF TEXAS AT ARLINGTON

August 2012

To my parents,

Who taught us more about the world

Than we could ever learn from a book,

While making the most of a life

About which others only read.

To my wife,

With whom any trial is made sweet,

Any victory more complete,

No story more vivid or cherished,

As the one we write together.

ACKNOWLEDGEMENTS

I would like to thank my supervising professor, Dr. Zdzislaw Musielak, whose knowledge, guidance, kindness, and apparently limitless patience were instrumental in both the progression of my research and my development as a physicist; Dr. John Fry for his expert advice and encouragement, and for always providing me with a new perspective; Dr. Andrew Brandt for giving me the singular opportunity to participate in experiments at labs in Europe and across the US; and Dr. Nail Fazleev, Dr. Chris Jackson, and Dr. Andrew White for taking the time to serve on my committee.

I would like to thank my loving and supportive wife, Rani, for encouraging and inspiring me, and for heroically maintaining her sanity during the unenviable task of being married to a physics grad student. I would like to thank my father Charles for teaching me the importance of both hard work and having fun; my mother Kathy for teaching me the values of curiosity and compassion; my brother Kevin for always helping me without once asking for anything in return; and all my family and friends whose love, support, and patience have somehow withstood my years of neglect as I pursued this dream.

Special thanks to Dr. Alex Weiss and the UTA Physics Department, the College of Science, the Graduate School, Dr. Nail Fazleev and the GAANN fellowship committee, and the US Department of Education (GAANN Grant No. P200A090284) for their continued financial support; and to Margaret Jackymack, whose daily battles with the second law of thermodynamics to keep the department in a solid state deserve the treatment of an epic poet.

July 20, 2012

ABSTRACT

QUANTUM MODELING OF DARK MATTER
IN GALACTIC HALOS

SHANE CHARLES SPIVEY, Ph.D.

The University of Texas at Arlington, 2012

Supervising Professor: Zdzislaw Musielak

Eighty years after its initial discovery, the nature of dark matter remains a mystery. Contrary to observational evidence, simulations of dark matter halos predict cuspy density profiles and an abundant population of dwarf galaxies. Increasingly refined measurements of the dark matter halos in galaxies reveal a large variety of halo shapes and sizes, and so far no universal profile has been able to incorporate them all. Among the numerous dark matter candidates, models of so-called quantum cold dark matter (QCDM) have the unique potential to address the many disparities between theory and observation.

QCDM postulates that dark matter is composed primarily of extraordinarily light (as small as $m \sim 10^{-24} eV$) bosonic particles. Such a small mass suggests a Compton wavelength on the order of parsecs, motivating the use of quantum mechanics on a galactic scale. Since dark matter by definition has no electromagnetic interaction, QCDM particles are bound to the lowest energy state of the galactic halo by a collectively-produced gravitational potential in the Schrödinger equation.

Thus in the first approximation a QCDM halo has the properties of a Bose-Einstein condensate, and the entire halo can be described by a single wave function.

In this dissertation, previous models of QCDM are reconsidered and compared to the most recent observational evidence. A comprehensive model for QCDM is then developed for a closed gravitational Schrödinger-Poisson system using the Hartree approximation. It is shown that the ground state solution to this system is well-approximated by an Einasto density profile with a shape parameter $n \approx 0.56$, which is a smooth-cored distribution.

The model is then expanded to include the influence of galactic baryonic matter distributions and the effects of a scattering potential, as well as excited and mixed-state dark matter halos. The addition of a black hole to the galactic potential is shown to produce a more concentrated halo with a cuspier core. The inclusion of a small-scale luminous matter distribution also concentrates the halo, while a large-scale distribution diffuses it; in either case the smooth core of the halo is preserved. The addition of a scattering term produces a rounder and more diffuse density profile; adding a sufficiently large black hole in combination with this term results in an even cuspier profile than the black hole alone. As a result of these additions, the model can be applied to a much larger range of halo shapes and sizes. Including excited states expands this range even further.

A comprehensive analysis of the theoretical framework is also presented, including a fully analytic power series solution to the gravitational Schrödinger-Poisson system. Finally, the Einasto density profile used as a fit for both simulated and observed dark matter halos is examined in depth, with emphasis on its significance to the models presented herein.

TABLE OF CONTENTS

LIST OF ILLUSTRATIONS

LIST OF TABLES

CHAPTER 1

INTRODUCTION

1.1 Brief History of Dark Matter Research

The first observational evidence for the existence of dark matter was found in the 1930s by astronomer Fritz Zwicky (Zwicky 1937). Zwicky was observing the rotations of galaxies inside the Coma cluster and noticed a peculiarity. Most of the ordinary matter in a galaxy is contained within its stars, and the light emitted by those stars can be used by astronomers to estimate the amount of such matter in a galaxy. More light means more stars, and more stars means more mass. If the locations and masses of galaxies inside a cluster are known, the virial theorem tells us how fast they should be rotating about the center of the cluster. What Zwicky discovered is that the galaxies were rotating at velocities not predicted by their calculated masses. He noted that in order to account for the discrepancy the galaxies must contain far more mass than what was actually observed. He dubbed this mysterious mass 'dark matter' because of its apparent lack of electromagnetic interaction. Since this dark matter did not emit light of any kind, its presence could only be inferred by its gravitational effects (Zwicky 1937; 1939; 1940; 1953).

Independent observational evidence for the existence of dark matter was found by astronomer Vera Rubin, who measured the rotation speeds of stars inside galaxies (Rubin et al. 1970). Using the virial theorem, the orbital speed of a star about the galactic center is determined by its radius of orbit and the mass profile of the galaxy. Based on the optically observed masses of the galaxies studied, stars located at the edge of a galaxy should have orbited with smaller velocities than those located

closer to the galaxy's center. What Rubin found instead was that the stars moved with approximately the same speed regardless of their orbital radius. To compensate for this difference, Rubin calculated that as much as 90% of the matter in galaxies must be unaccounted for. Connecting this idea with Zwicky's earlier discovery, she concluded that this missing mass could in fact be dark matter (Rubin et al. 1970; Rubin et al. 1980).

Additional strong evidence for the existence of dark matter was given by NASA's WMAP (e.g. Bennett et al. 2003; Spergel et. al 2003; Komatsu et al. 2011) and by some gravitational lensing measurements (e.g., Ellis 2010). Using the WMAP data, the total amount of dark matter in the Universe was established. The actual value is $\Omega_M = 0.27 \pm 0.04$ and it includes both the visible and invisible (dark) matter, with the former being only a very small fraction of the latter (e.g., Komatsu et al. 2011). Astronomical data seemed to also imply that more than 80% of dark matter is non-baryonic cold dark matter of unknown identity. Since the remaining energy content is the so-called dark energy, $\Omega_\Lambda = 0.73 \pm 0.04$, the astronomical observations clearly show that most mass in the Universe is in the form of cold dark matter (Livio 2004).

For decades, researchers have proposed numerous models in an attempt to explain dark matter and describe its properties. These models include an alternative to dark matter proposed in 1983 by Mordehai Milgrom (Milgrom 1983). Milgrom's theory, called Modified Newtonian Dynamics (MOND), attempts to reconcile the galactic rotation curve problem by modifying Newton's law of gravity. Later studies of gravitational lensing in galaxy clusters seemed to rule out MOND as a viable theory (Markevitch et al. 2004), though others have disputed that claim (Angus et al. 2006; Bekenstein 2006; Milgrom 2011). In the decades since Milgrom's initital proposal the evidence against it has continued to mount (e.g., Aguirre et al. 2001; Clowe et al.

2006; Famaey et al. 2007; Wojtak et al. 2011). Today, the near consensus among astronomers is that most of the dark matter in the universe is nonrelativistic, or *cold*, (e.g., Copi et al. 1995; Bergstrom 2000; Garrett and Duda 2011), but the search for the exact nature of the elementary dark matter particle is still ongoing (e.g., Bertone et al. 2005).

1.2 Evidence for Dark Matter

The two primary bodies of evidence for dark matter come from studies of the rotation curves in galaxies and the gravitational lensing of clusters.

1.2.1 Galactic Rotation Curves

The most important evidence for dark matter in galaxies comes from the analysis of stellar orbital velocities (Bertone et al. 2005). According to Newtonian dynamics, the velocity of an object in a nearly circular orbit is

$$v^2 = \frac{GM(r)}{r}, \tag{1.1}$$

where r is radius of the orbit, $M(r)$ is the total mass contained within that radius, and G is the universal gravitational constant. If the mass density profile $\rho(r)$ of the system is known, then the total mass $M(r)$ can be found by

$$M(r) = \int_0^r r'^2 \rho(r') dr'. \tag{1.2}$$

The graph of v(r) is often called the galactic rotation curve (or sometimes velocity curve). If only the mass of the baryonic matter in a galaxy is considered, the Newtonian equations suggest that the rotation curves in most galaxies should decrease with increasing distance from the galactic center. Instead, what astronomers have found is that most galaxies have relatively flat rotation curves, meaning that stars at the fringes of a galaxy orbit at nearly the same velocity as stars closer in

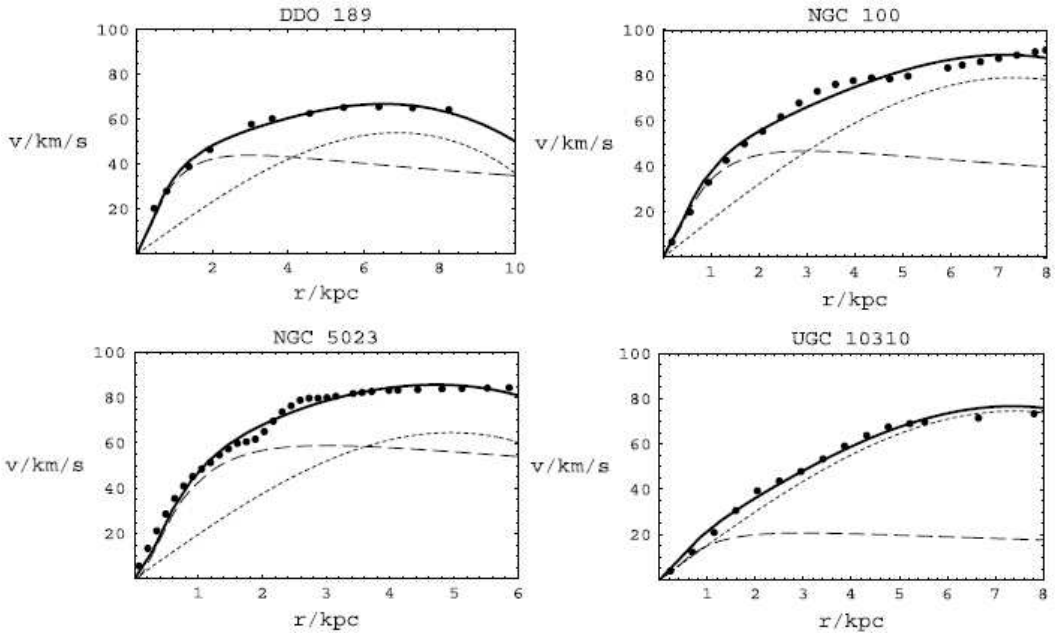

Figure 1.1. Radial velocity curves for several real galaxies (Bohmer and Harko 2007).

(e.g., Rubin et al. 1980; de Blok and Bosma 2002; Battaglia et al. 2005; Brown et al. 2007; Read et al. 2007; Chemin et al. 2011).

Figure 1.1 shows rotation curves for several real galaxies. The dashed curves represent the Newtonian values where only the baryonic matter in each system is included in the mass calculation. The dots are the actual observed velocity values of stars in these systems. The solid lines represent the Newtonian values after a simulated dark matter halo has been added to the system. These plots demonstrate that observed rotation curves can be accounted for by assuming a halo of dark matter exists in each galaxy (Bohmer and Harko 2007).

1.2.2 Gravitational Lensing

Another strong piece of evidence for dark matter comes from studies of gravitational lensing. According to Einstein's Theory of General Relativity, massive systems such as galaxy clusters exert a gravitational force on photons, bending their paths in

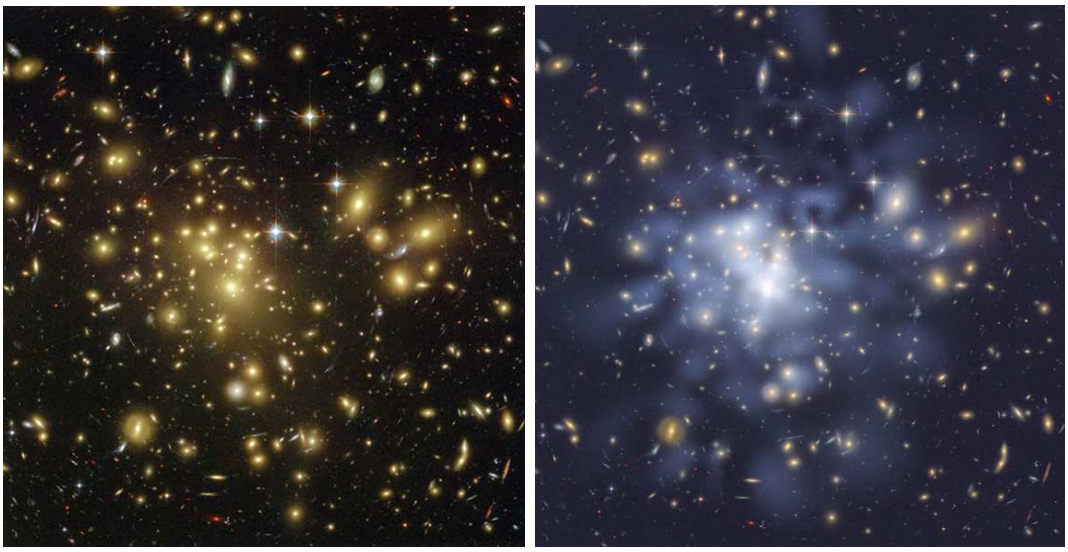

Figure 1.2. Galaxy Cluster Abell 1689 in the visible range only (left) and with the dark matter distribution superimposed in blue (right). The dark matter data was inferred from weak gravitational lensing studies (NASA Image).

a predictable way. This bending of light rays causes a distortion in the background image similar to that created by a lens (Einstein 1936; Schneider and Weiss 1988). By observing these distortions, astronomers can determine the approximate amount and distribution of mass that should be found in a particular galaxy cluster. Just as with rotation curves, gravitational lensing studies have shown that there is much more mass in galaxies than is indicated by their luminosity (Blandford and Narayan 1992; Bartelmann and Narayan 1995; Ellis 2010).

The bending of the light ray is greater the closer it passes to the source mass. If the light source and the observer are mutually aligned with the lensing object, the light will appear as a ring around the mass (called an Einstein Ring). In less symmetric cases, the observer may see multiple arcs or distorted images of original light source. These are examples of so-called strong lensing, where the distortion is readily apparent. Smaller distortions are referred to as weak lensing.

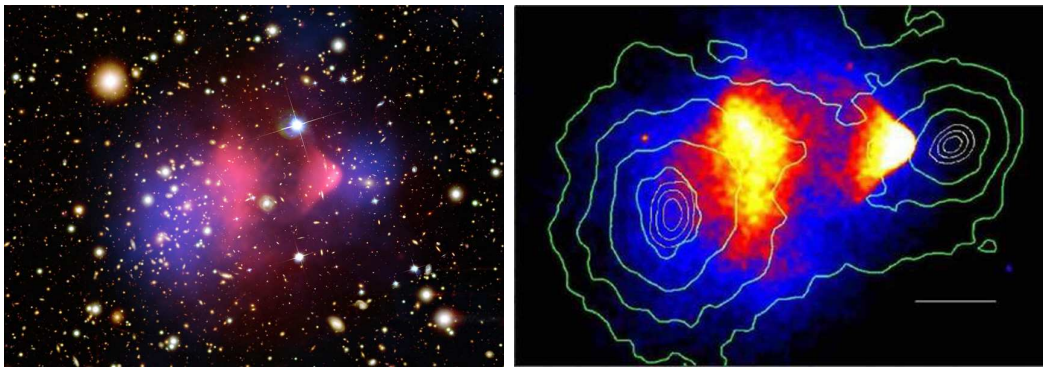

Figure 1.3. The Bullet Cluster with dark matter in blue and the hot gases in red. The figure on the right includes a contour map of the total mass. The stellar and dark matter passed though the collision together, while the interacting hot gases lag behind (NASA Image).

Weak lensing studies have been used to create maps of dark matter in galaxy clusters (e.g., Bartelmann and Narayan 1995; Taylor et al. 2004; Massey et al. 2007). When light from distant source galaxies passes through the cluster, these galaxies appear stretched in a direction perpendicular to the center of the cluster's gravitational field (see Figure 1.2). By analyzing the amount and orientation of this stretching over a large number of source galaxies, astronomers can determine the mass distribution inside the cluster.

One particularly dramatic piece of evidence for dark matter using gravitational lensing is the so-called Bullet Cluster (Figure 1.3), which is actually two clusters in the process of merging (Tucker et al. 1998). Galaxy clusters typically contain hundreds of galaxies disbursed within a large intergalactic medium of ionized gas and dark matter. The stellar content of a cluster is sparsely distributed within its galaxies. Because the stars are electrically neutral and spread so thinly, two clusters can pass through one another with almost no interaction between their stars, leaving their stellar distributions unperturbed. On the other hand, the more uniformly distributed ionized gases (shown in red in Figure 1.3) have a much closer approach distance and

interact electromagnetically. Observations of the Bullet Cluster from the Chandra X-ray observatory (Markevitch et al. 2004; Clowe et al. 2006) confirm that while the stellar matter from each cluster passed through undisturbed, the hot gases collided and lagged behind. Gravitational lensing indicates that the dark matter content (shown in blue in Figure 1.3) followed the stellar component, reconfirming that it too is electrically neutral. It also suggests that dark matter is more bound to the matter in galaxies rather than to the intergalactic medium.

1.3 Dark Matter Candidates

1.3.1 Hot Dark Matter

Hot dark matter refers to particles which travel at ultrarelativistic velocities. The most common hot dark matter candidate is the neutrino (Dolgov 2002). Neutrinos have a very small mass (less than a millionth of an electron) and have no electromagnetic interaction, making them very difficult to detect. It's likely that hot dark matter makes up only a tiny percentage of the total dark matter content of the universe (Bertone et al. 2005). Dark matter particles moving at relativistic speeds cannot slow down enough to bind gravitationally to one another at a small scale. Dark matter's role in small scale structure formation is key to understanding how galaxies first formed after the Big Bang (Demiaski et al. 2011).

A subcategory exists for so-called warm dark matter particles which would travel at lower relativistic velocities. No observed candidates exist in this range, but there is one postulated particle known as the sterile neutrino (Bertone et al. 2005; Sugita et al. 2008).

1.3.2 Cold Dark Matter

Cold dark matter (CDM) particles move at subrelativistic speeds, permitting small scale structure. Under the CDM paradigm, small clumps of dark matter eventually undergo gravitational collapse and then bind with more objects in a continuous hierarchical process, creating more and more massive structures over time. In contrast, hot dark matter models require top-down structure formation, where superclusters form first and split into smaller structures over time (White and Frenk 1991; Demiaski et al. 2011; Wang et al. 2011). The current consensus among cosmologists is that only CDM theory can explain current observations, including both large-scale structure of the universe and gravitational lensing in galaxy clusters (Copi et al. 1995; Bertone et al. 2005; Garrett and Duda 2011).

Some of the first proposed CDM candidates were Massive Compact Halo Objects, or MaCHOs. These are large astrophysical objects such as black holes, neutron stars, and white dwarfs, all of which are thought to populate the galactic halo. Since these objects give off little or no light, they are a baryonic form of dark matter. MaCHOs appear to make up only a small percentage of the dark matter in individual galaxies (Tisserand et al. 2007).

A more recently postulated source of large-scale dark matter called RAMBOs (Robust Associations of Massive Baryonic Objects) would consist of a star cluster made of brown or white dwarfs. Like MaCHOs, RAMBOs give off little or no light and could be long-lived and dynamically stable, but there would not be enough of them to account for the majority of dark matter (Moore and Silk 1995).

More promising are the particle candidates which often arise naturally as extensions to the Standard Model of particle physics (Ellis and Olive 2010). One such particle is the axion (Asztalos et al. 2001; Sikivie 2008), initially proposed as a solution to the strong CP problem of Quantum Chromodynamics. Axions would have

very low mass, less than 1 eV, and have self-interaction characteristics that would make them a viable candidate for dark matter. Axions have so far not been detected (Rosenberg and Bibber 2000; Sikivie 2008).

One of the most popular candidates is the Weakly Interacting Massive Particle, or WIMP. WIMPS interact only with gravity and the weak nuclear force and have an expected mass on the order of GeV, making them not much heavier than a proton (Bertone et al. 2005; Barbier et al. 2005; Garrett and Duda 2011). A number of experiments are currently searching for evidence of WIMPs . Some look for neutrino emissions caused by WIMP annihilations in the Sun, such as Japan's Super-Kamiokande detector, or from the galactic center (Bertone et al. 2005; Fernengo 2008). Some more direct detection methods include the Cryogenic Dark Matter Search (Ahmed et al. 2011), which looks for WIMPs colliding with a crystal matrix; the Canadian PICASSO project (Archambault et al. 2009), which uses a principle similar to a bubble chamber; and the Italian WARP (Acosta-Kane et al. 2008), which looks for scintillating light pulses caused by WIMPs passing through liquid Argon. WIMPs have not yet been definitively observed (Bertone and Merritt 2005; Fornengo 2008).

A leading WIMP candidate is the neutralino, a particle predicted by the supersymmetry extension of the Standard Model. Like a neutrino, it would interact via the gravitational and weak forces, but it's mass should be in the range of 10-1000 GeV. The neutrino-nucleon weak interaction scale is high enough that it is expected to have a measurable interaction with target materials used in WIMP detectors (Feng 2010).

As successful as CDM theory has been, not all of its predictions are borne out by observations. There are two main problems to be overcome in CDM theory (Copi

et al. 1995; Bergstrom 2000; Bertone et al. 2005; Navarro et al. 2010; Garrett and Duda 2011; Ferrero et al. 2011):

- CDM simulations predict far more dwarf satellite galaxies than have been observed so far. One possible solution to this is that most of the missing dwarf galaxies are actually low surface brightness (LSB) galaxies, where the mass to light ratio is in the neighborhood of 1000 or more. Such galaxies are made up almost entirely of dark matter, making them nearly invisible (Hayashi et al. 2004). Eight such galaxies were found orbiting the Milky Way by astronomers at the Keck Observatory in 2007 (Simon and Geha 2007). Another possibility is that most dwarf satellites end up being tidally stripped by their parent galaxies (Kazantzidis et al. 2003).
- CDM simulations produce dark matter halos whose density profiles are highly peaked or 'cuspy' at the core. The exact nature of core behavior is unknown, but observations of galactic rotation curves suggest less sharply peaked central density profiles in most large halos, and much flatter cores for smaller galaxies (de Blok 2010). Unless either the simulations or the observations are wrong, this problem can only be reconciled by a modification to the theory (Mcgaugh et al. 2003).

  Resolving these problems is the next important hurdle in the study of CDM.

1.3.3 Quantum Cold Dark Matter

The CDM predictions of highly cusped halo profiles and an abundance of low mass halos continue to plague an otherwise successful model. Different ideas have been put forward to resolve these discrepancies (e.g., Hu et al. 2000; Cheng et al. 2002; Albuquerque et al. 2003; Navarro et al. 2010, and references therein). One possible solution is to postulate the existence of an extraordinarily light particle (ELBP) with

a mass on the order of 10^{-24} eV (Sin 1994) or 10^{-22} eV (Hu et al. 2000). As originally noted by Sin (1994), such a small mass has a Compton wavelength on a galactic scale of 10 pc or more. In this context, a quantum mechanical treatment is necessary. For this reason, ELBPs are sometimes called 'fuzzy' cold dark matter (FCDM) or quantum cold dark matter (QCDM). In a quantum treatment the wave functions of the individual particles in such a dark matter halo are overlapping. If the particles are bosons, it has been postulated that such a configuration constitutes an enormous Bose-Einstein condensate on the scale of the entire galaxy (e.g., Bohmer and Harko 2007). Formation of large-scale structures with the ELBPs was investigated by Woo and Chiueh (2009).

1.4 Density Profiles of Galactic Halos

Observational evidence suggests that dark matter halos are approximately spherical (Burkett 1995; Ackermann et al. 2011; Chemin et al. 2011; Salvador-Sole et al. 2011). Several groups (e.g., Klypin et al. 2002; Xue et al. 2008; McMillan 2011) have studied the dark matter halo of the Milky Way, which is a large spiral galaxy, and found an overall mass in the range of 10^{12} solar masses and a virial radius on the order of $200 - 300$ kpc. Large elliptical galaxies have both hot gas halos and dark matter halos, with the former being bound to the galaxies by the latter (e.g., Baes and Dejonghe 2001). Dark matter halos of dwarf galaxies, which are either spiral, elliptic or irregular, are in general much denser than those observed around large galaxies (e.g. Ferrero et al. 2011). There is now evidence of a special kind of dwarf galaxy called an ultrafaint or low surface brightness (LSB) galaxy that contains very few stars at all. Such galaxies are almost completely dominated by dark matter. Several LSB dwarf galaxies were recently discovered around the Milky Way and Andromeda

(Belokurov et al. 2010; Collins et al. 2010). Stellar and halo masses of some Local Group galaxies were recently given by Li and White (2008).

Density profiles of dark matter galactic halos are typically deduced from N-body numerical simulations in which the dark matter particles are treated classically (e.g., Navarro et al. 2010; Ludlow et al. 2011). Depending on the specific assumptions used in those simulations, different density profiles can be produced. Examples of such profiles include: the Einasto profile (Einasto and Haud 1989; Merritt et al. 2005; Einasto 2011), the Navarro-Frenk-White (NFW) profile (Navarro et al. 1996, 2010), and the modified isothermal profile (Burkert 1995; Bergstrom et al. 1998). All three profiles have two scale parameters which can be modified to accommodate halo size, but only the Einasto profile contains an additional shape parameter n, making it adaptable to different halo types.

Chemin et al. (2011) recently fit a number of observed galactic halos to Einasto profiles with different n values. Their results indicate that the values of n may range from 0.1 to more than 10. Although there is a great deal of variation, larger halos typically have larger values of n, while dwarf galaxies tend to have the smallest n values. For the latter, the inner profiles are shallow and core-dominated, which indicates that $n < 1$. According to Navarro et al. (2010), the Einasto profile with n varying from one galaxy to another represents the best overall fit for the density profiles of dark matter halos. Another conclusion of the Navarro et al. paper is that these profiles are not universal, which means that different halos cannot be rescaled to look the same.

1.5 Objectives of This Dissertation

The main objective of this dissertation is to reconsider the QCDM model originally introduced by Sin (1994) and later modified by Hu et al. (2000), to test its

validity by imposing astronomical constraints (Spivey et al. 2012), and to explore ways to expand its applicability. Since the model is based on the Schrödinger equation with a gravitational potential term, this equation will be solved on a galactic scale by using established astronomical data for the Milky Way and a dwarf galaxy. The results are compared to the obtained solutions for different Einasto density profiles in order to find the value of the index n that is consistent with both the astronomical data and the QCDM model.

Since both the Sin and Hu et al. models are formally considered, their respective values for masses of the ELBPs, namely, 10^{-24} eV and 10^{-22} eV, will be used in these computations; note that the latter value was also used in the numerical simulation performed by Woo and Chiueh (2009). The results of these computations demonstrate that the models reproduce well the Einasto profile with an index of $n \approx 0.56$; essentially, the same result is obtained by a self-consistent model, which is also considered here. One important result is that the Sin and Hu et al. models cannot account for the total mass and size of the dark matter halos of two different galaxies, such as the Milky Way and a dwarf galaxy. This clearly shows the limitation of the QCDM models when restricted to a single bosonic particle mass. The results presented in this dissertation will establish the conditions under which the current QCDM models are valid and provide several possible improvements to the models that could potentially overcome these shortcomings.

In the next chapter, the QCDM models are explored and tested for their compatibility with commonly used halo density profiles for a range of established astronomical values. In addition, a self-consistent QCDM model is similarly explored. In Chapter 3 the model is expanded to include external potentials.

CHAPTER 2

DARK MATTER IN THE QUANTUM REGIME

2.1 Quantum Models of Cold Dark Matter

In the QCDM models considered by Sin (1994) and Hu et al. (2000), the dark matter (DM) particles are identical bosons (ELBPs) with spin zero and masses small enough to motivate their description by non-relativistic quantum theory. As mentioned in the previous chapter, one primary difference between the models is the assumed mass of the ELBPs. According to Sin (1994), this mass should be on the order of 10^{-24} eV, while Hu et al. assumed a mass on the order of 10^{-22} eV.

Both models are based on the assumption that the particles interact with each other only gravitationally and that they are represented by scalar wave functions which are solutions to a Schrödinger equation with a gravitational potential term. The Schrödinger equation is solved on a galactic scale, and the ELBPs form a galactic DM halo, which is assumed to be spherical. Any contribution of the galactic visible matter is neglected because it is small when compared to the DM halo. Clearly, the models are simple, and yet they do appear to resolve the classic CDM problems of overly cuspy halo profiles and an abundance of low mass halos (Sin 1994; Hu et al. 2000).

The compatibility of these models with commonly used halo density profiles for a range of established astronomical values has been explored by Spivey et al. (2012). The paper also presents a self-consistent Schrödinger-Poisson model. The main results of this paper are now presented and discussed.

The ELBPs are described by a scalar wave function ψ, which obeys the standard time-independent Schrödinger equation

$$E\psi = -\frac{\hbar^2}{2m}\nabla^2\psi + V(\mathbf{r})\psi \ , \tag{2.1}$$

where $\hbar$ is the Planck constant, m is the mass of the bosonic particles and $V(\mathbf{r})$ is a potential to be specified.

The gravitational potential created by a distribution of mass is given by the Poisson equation. Then for a particle of mass m in a radially symmetric halo of dark matter,

$$\nabla^2 V(r) = 4\pi G m \rho_{\rm DM} \ , \tag{2.2}$$

where G is the gravitational constant, $\rho_{\rm DM} = M|\psi|^2$ is the density of the dark matter halo, and M is a the total mass of the halo. The effects of incorporating the galaxy's visible (luminous) matter $\rho_{\rm LM}$ into the potential will be examined in Chapter 3. Because $\rho_{\rm LM} << \rho_{\rm DM}$ for most galaxies, it is neglected in this chapter. In the approach presented by Hu et al., $\rho_{\rm dark} = m^2|\psi|^2/2$ and $\rho_{\rm visible}$ is also neglected.

The physical problem represented by Eqs. (2.1) and (2.2) is that of an ensemble of mutually interacting particles in a potential well of their own making. The particles' behavior in the well is described by solutions to a nonlinear Schrödinger equation.

2.2 Analysis Using Established Density Profiles

In order to test the range of validity for the DM models described in Sec. 2.1, real astronomical data can be used to constrain the physical parameters of the system, and the results can be compared with some empirically obtained halo density profiles. Such profiles are typically obtained from N-body numerical simulations (e.g., Navarro et al. 2010). However, recent results from Chemin et al. (2011) show that they can also be established by direct observations of galactic rotation curves. This section will

examine three of the most commonly used density profiles: the Navarro-Frenk-White (NFW) profile, the modified isothermal (ISO) profile, and the Einasto profile, with particular emphasis on the latter.

Developed by Navarro, Frenk and White (Navarro et al. 1996, 2010) as a best-fit model for their dark matter simulations, the NFW profile is one of the oldest and most commonly used density profiles for modeling dark matter halos (Bertone et al. 2005). It is given by $\rho(r) = \rho_{crit}\delta_c/[(\frac{r}{R_s}(1+\frac{r}{R_s})^2)]$, where $R_s = r_{vir}/c$, ρ_{crit} is the critical density of the universe, and δ_c is the characteristic overdensity, which depends on the concentration parameter c. For spiral galaxies, N-body simulations suggest a c about 12 (Merritt et al. 2006).

Several studies have also been made modeling dark matter halos using the ISO profile (Burkert 1995; Bergstrom et al. 1998), which is smooth-cored in contrast to the cuspy NFW profile. It is given by $\rho(r) = \rho_0/(1+(\frac{r}{R_s})^2)$, where $\rho_0 = \rho(r=0)$, and the scale radius is defined by $\rho(r = R_s) = \rho_0/2$.

The Einasto profile comes from Sérsic's Law (Sérsic 1963), which describes how the intensity of a galaxy changes with the distance from its center. Recently, the Einasto profile has been more frequently used as a mass density profile in DM simulations, with much success (Einasto and Haud 1989; Haud and Einasto 1989; Merritt et al. 2006; Navarro et al. 2010). The profile is given by

$$\rho(r) = \rho_{1/2}\ e^{-d_n[(r/r_{1/2})^{1/n}-1]}\ , \tag{2.3}$$

where $r_{1/2}$ is the median of the halo or the radius that encloses half the total mass, $\rho_{1/2}$ is the density at $r_{1/2}$, d_n is a unitless parameter which depends only on n, and $n > 0$ is a real number. The parameter n describes the steepness of the curve.

Ground state solutions of the time-independent Schrödinger equation can be found by starting with a state function ψ and separating the independent variables

by writing $\psi(r,\theta,\phi) = R(r)Y_l^m(\theta,\phi)$. The ground state solution occurs when the angular function is ${Y_0}^0(\theta,\phi) = \frac{1}{\sqrt{4\pi}}$, and the resulting radial Schrödinger equation can be written as

$$\nabla^2 R(x) = \left[\frac{2G}{\hbar^2}\rho_0 m^2 {r_s}^4 V(x) - {r_s}^2 \frac{2mE}{\hbar^2}\right] R(x), \tag{2.4}$$

where r_s is some suitable scale radius, $x = r/r_s$, and $V(x)$ is the potential from Eq. (2.2), stripped of all constants.

By assuming that one of the given density profiles already represents the distribution of quantum DM particles, this distribution can be used in Eq. (2.2) to generate the gravitational interaction of a DM particle with the average potential produced by all other DM particles. Because the interaction between a pair of DM particles is extremely weak, it is a good first approximation to neglect other many body effects. With the assumption that this Hartree approximation (Merzbacher 1997) is valid for the DM many body problem, the Schrödinger equation with the given potential $V(x)$ can be solved and the resulting probability densities can be directly compared to the NFW, ISO, and Einasto density profiles.

2.2.1 Results

As an example, take the Einasto profile with $n = 1$ (see Eq. 2.3), which yields

$$\rho(x) = \rho_0 e^{-x} \ , \tag{2.5}$$

where $x = d_1(r/r_{1/2})$, $\rho_0 = \rho_{1/2}\ e^{d_1}$ and $d_1 \approx 2.67457$. The potential $V(x)$ resulting from the above density profile is

$$V_{Ein}(x) = \frac{e^{-x}(x+2) - 2}{x} \ . \tag{2.6}$$

Solving Eq. (2.4) with this potential, the resulting probability density can be compared with the Einasto profile given by Eq. (2.5). The results are plotted in the

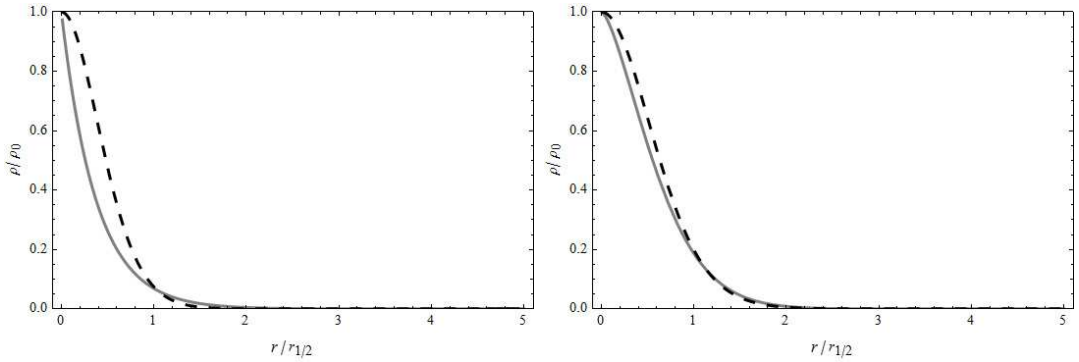

Figure 2.1. Einasto density profiles (solid) and the resulting probability densities (dashed) corresponding to the ground state for $n = 1$ (left) and $n = 2/3$ (right). Each density ρ is plotted in terms of its core value ρ_0, with r being measured in terms of the halo median $r_{1/2}$ (Spivey et al. 2012).

left panel of Figure 2.1, and it can be seen that the probability density produced by the Schrödinger equation is not a good fit for the Einasto profile with $n = 1$.

Next, a similar computation is performed with a value of $n = 2/3$. Obtaining the potential $V(x)$ for this density profile and solving the Schrödinger equation with it yields the results in the right panel of Figure 2.1, which shows that the agreement is better but not yet good enough. The desired value of n is the one that best fits the probability densities computed from the Schrödinger equation to the Einasto density profile. Based on the results presented in the left and right panels of Figure 2.2, the best fit is obtained for $n \approx 0.56$ (Spivey et al. 2012). For comparison, the results for the same analysis with the NFW and ISO profiles are shown in Figure 2.3.

The potential produced by a finite density distribution via the Poisson equation must be a continuous function with a continuous derivative. It is therefore subject to the boundary condition $V'(0) = 0$, which means the resulting potential will have a 'smooth' or shallow region near the origin. As a result, solutions to the Schrödinger equation for such potentials will tend to also have a shallow region very near the core. This behavior is further examined in Chapter 5.

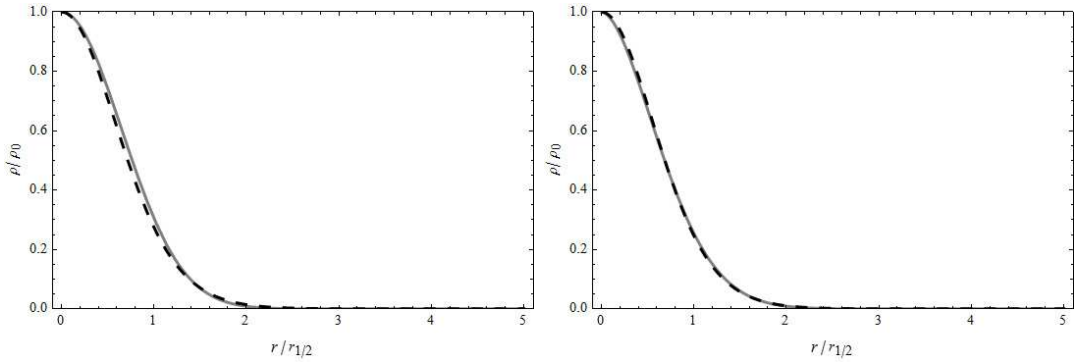

Figure 2.2. Einasto density profiles (solid) and the resulting probability densities (dashed) corresponding to the ground state for $n = 0.5$ (left) and $n = 0.56$ (right). Each density ρ is plotted in terms of its core value ρ_0, with r being measured in terms of the halo median $r_{1/2}$ (Spivey et al. 2012).

The effect is most evident when examining the NFW input and output densities in Figure 2.3. The NFW profile has a singularity at the origin, giving it infinite density there. When used as a fit for simulations, it is always resolved to a nonzero inner radius to avoid this problem (Navarro et al. 1996). Despite its highly peaked core, the wave function produced by its potential still has a flat core with a finite value (Spivey et al. 2012).

Both the NFW and ISO profiles also have mass functions that diverge as $r \to \infty$. In order to retain a finite mass, a radius must be selected as a cutoff point where the halo is considered to be virialized. Typically, a virial radius of $r_v = r_{200}$ is selected, where r_{200} is the radius at which ρ_{DM} equals 200 times the critical density of the universe (Navarro et al. 1996; Bergstrom et al. 1998; Merritt et al. 2006).

The Einasto profile, by contrast, is well-behaved at both the origin and infinity. While the NFW and ISO profiles take the form of broken power laws, the Einasto density profile decays as an exponential of power of r, ensuring a finite mass and density over all space. This suggests the Einasto profile is a more natural fit for a quantum probability density, which can never be infinite and must always be normalizeable to

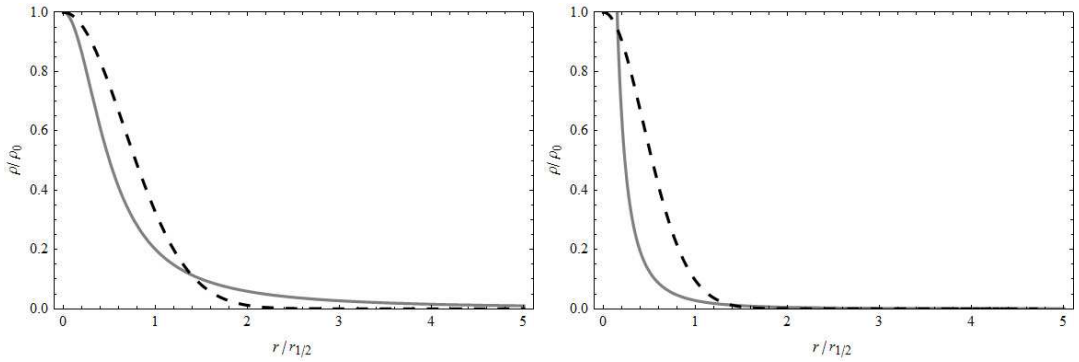

Figure 2.3. Density profiles (solid) and the resulting probability densities (dashed) corresponding to the ground state for the modified isothermal profile (left) and the NFW profile (right). Each density ρ is plotted in terms of its core value ρ_0, with r being measured in terms of the halo median $r_{1/2}$ (Spivey et al. 2012).

1. In addition, observational evidence (Chemin et al. 2011) and recent simulations (Navarro et al. 2010) have singled out the Einasto profile as the best overall fit for the density profiles of dark matter halos.

In all the results shown in Figures 2.1 and 2.2, the plotted probability densities and the Einasto density profiles scale with the physical parameters of the system, mass and radius, which means that they are scale independent and therefore valid for both QCDM models considered here. It is important to note that the probability densities shown by dashed lines in Figures 2.1 and 2.2 represent ground states and that these states were found for masses given by the Sin and Hu et al. models.

In every case, the solutions to the Schrödinger equations yield a direct relationship between the halo parameters: total halo mass M and median radius $r_{1/2}$, and the mass m of ELBPs. The relationship is given by

$$M r_{1/2}\, m^2 = c_n, \tag{2.7}$$

where c_n is a constant value which varies slightly for each n (Spivey et al. 2012).

If the bulk of a halo is comprised of a single type of particle with a given mass m, the above relations would imply that the median of any halo is inversely proportional to its mass. This contradicts most simulations, which are based on a distribution of classical particles. However, recent observations of galaxy cluster A 1689 (Navarro et al., 2010) reveal a halo far more centrally concentrated than simulations predict. This data comes from observations of gravitational lensing, which give an actual picture of the halo. Data for galaxy halos is based on rotation curves, so halo shapes on the galactic scale are inferred rather than seen. Moreover, it should be noted that the median of a galactic halo does not reflect its overall radius of influence, which depends on both the shape and density parameters. An arbitrary cutoff point can be selected when the density dips below a certain value, but since the impact of such a cutoff on these results would be insignificant, it is not considered here.

Now, Hu et al. (2000) assumed a 10^{-22} eV particle using a method designed to eliminate the cuspy halo core. Sin (1994) suggested a mass of 10^{-24} eV, with the caveat that the particle cannot be in the ground state. Figure 2.2 shows that a stable ground state solution exists for a halo resembling an Einasto density profile. Estimated values for halo mass M and median $r_{1/2}$ for the Milky Way and a dwarf galaxy (based on observations or numerical simulations of their galactic dark matter halos) can be found in the literature. These values can be plugged into Eq. (2.7) to determine the range of validity for the established values of m.

For the Milky Way galaxy, Klypin et al. (2002) have limited the practical range of the halo mass M to be between 0.5×10^{12} and 2×10^{12} solar masses. According to numerical simulations, the virial radius of such a halo is on the order of 200 to 300 kpc. Since the Einasto profile decays exponentially out to infinity, it uses the halo median $r_{1/2}$ as its scale radius. The above limitations on the virial radius give an overall median spread of around $50 - 200$ kpc, which will be used as the practical

boundaries for the Einasto profile of the Milky Way. Using the relationship given by Eq. (2.7) and taking $M = 1.0 \times 10^{12}$ solar masses, the median is found to be $r_{1/2} = 3.4$ kpc and the viral radius 18 kpc for $m = 1.0 \times 10^{-24}$ eV; note that the values of $r_{1/2}$ and virial radius are an order of magnitude below the observationally established values. Attempting to take the same M but with $m = 1.0 \times 10^{-22}$ eV yields a vanishingly small median of $r_{1/2} < 1$ parsec (Spivey et al. 2012). The desired median range is found when $m = (1.3 - 2.6) \times 10^{-25}$ eV, which is a much lower mass than that considered by Sin (1994) and Hu et al. (2000).

Next consider an elliptical dwarf galaxy with mass on the order of $M = 10^9$ solar masses and a median in the range of $r_{1/2} = (0.1 - 10)$ kpc (Graham et al. 2006). Using Eq. (2.7) with $M = 1.0 \times 10^9$ solar masses results in $r_{1/2} = 0.34$ kpc for $m = 1.0 \times 10^{-22}$ eV; similar analysis performed for $m = 1.0 \times 10^{-24}$ eV puts $r_{1/2}$ four orders of magnitude larger, well outside the range of likely values for this or any other dwarf galaxy (Spivey et al. 2012).

The results presented above have important implications as they clearly show that the QCDM models with a given mass developed by Sin (1994) and Hu et al. (2000) cannot explain DM halos of different galaxies. The best these models can do is predict the total mass and size of the DM halo for a particular galaxy by tuning the value of mass for the ELBPs. Changing the particle mass to fit each individual halo would contradict the very basic assumptions made in the models. This is an important limitation, and it suggests a more complicated picture may be needed.

2.3 Self-consistent Schrödinger-Poisson Model

A second method is to proceed as in the previous section but without the assumption that the density must be described by a known density profile. Instead, the mass density in Eq. (2.2) can be replaced directly with $\rho_{\rm DM} = M|\psi|^2$. Eqs.

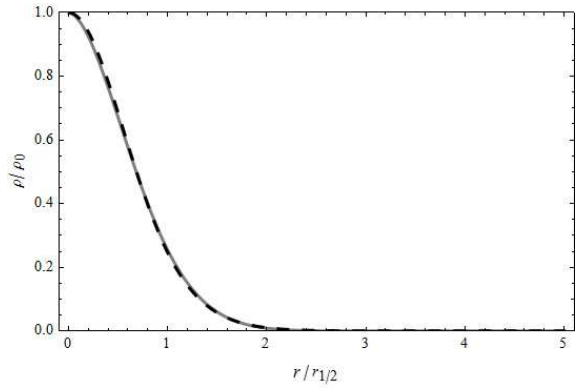

Figure 2.4. Ground state probability density for the self-consistent Schrödinger- Poisson system (dashed) and the Einasto density profile for $n = 0.56$ (solid). Each density ρ is plotted in terms of its core value ρ_0, with r being measured in terms of the halo median $r_{1/2}$ (Spivey et al. 2012).

(2.1) and (2.2) can then be solved as a set of coupled nonlinear differential equations. The ground state solution to this Schrödinger-Poisson system is shown in Figure 2.4. Fitting this solution to an Einasto distribution gives $n \approx 0.56$, and Figure 2.4 shows the excellent agreement between these densities (Spivey et al. 2012).

As before, the result is independent of the halo parameters of mass and median, as well as the particle mass. For both methods, the product of these values is fixed for the ground state, so that an increase in one results in a decrease of one or both of the others. If the particle mass is to remain invariant, then there is an inverse relationship between the mass of a halo and its median.

This interesting result reflects the fact that the ideal solution to the problem of *what density distribution reproduces itself* is limited by its own geometry. A mass density entered in the gravitational Poisson equation will produce a unique potential, and that potential will produce a unique set of orthogonal eigenstates via the Schrödinger equation within the Hartree approximation. Of these, only the ground state has been considered thus far.

It should be noted that in this chapter the term *ground state* has been in reference to the *nodeless* solution, in analogy with known linear quantum systems such as the hydrogen atom. In fact, any change at all to the potential produces a technically different complete set of solutions, but each set produces one solution with no nodes. The assumption that the nodeless solution refers to the lowest energy, or ground, state is explored in Chapter 4. The possibility of halo wave functions with nodes, as well as halos with a mix of states, is also discussed in that chapter.

The halo parameters depend in part on the selected particle mass. For example, a 10^{-24} eV particle as proposed by Sin (1994) fits reasonably well with a halo of mass 10^{11} $M_{\rm sun}$ and median on the order of 30 kpc, while a 10^{-22} eV particle, as suggested by Hu et al. (2000) might better describe a 10^{8} $M_{\rm sun}$ mass halo with a median on the order of 3 kpc. As already discussed in Sec. 2.2, the fact that ELBPs of different masses are needed to account for DM halos of different galaxies is a major problem of both QCDM theories (Spivey et al. 2012).

2.4 Summary

In this chapter, two previously developed QCDM models were reconsidered against the most recent observational data on dark matter halos. The models are based on the Hartree approximation and on the assumption that the particles interact with each other only gravitationally. Moreover, contributions of the galactic visible matter are neglected. Despite their simplicity, the models do produce halos with flatter central densities than those created by simulations, somewhat alleviating the cuspy core problem of CDM. In addition, QCDM models can provide an elegant explanation the existence of stable, dark matter-dominated halos. Many such halos are now known to populate the fringes of the Local Group (Belokurov et al. 2010; Collins et al. 2010).

To determine the validity of the models, several halo density profiles were computed for a gravitational Schrödinger-Poisson system. Using the models' predicted particles masses of 10^{-24} eV and 10^{-22} eV and halo physical parameters deduced from observational data, the resulting density profiles were compared to known density profiles used to model real dark matter halos. The results demonstrate the following:

- The QCDM models produce an Einasto density profile with $n \approx 0.56$. This makes the model most appropriate for dwarf galaxies, which can be fit to Einasto profiles with $n < 1$ (Chemin et al. 2011).
- The models cannot account for the variety of halo shapes actually observed. Like the NFW and modified isothermal profiles, the ground state QCDM density does not change its shape based on the mass or size of the halo. Since larger galaxies can be fit to Einasto distributions with higher n values, this limits the scope of these models.
- The QCDM models also cannot account for the size and total mass of observed halos without invoking a different particle mass for each halo.

Considering the successful application of the Einasto profile in describing both observed and simulated dark matter halos, the fact that a QCDM model can produce such a profile suggests it is worthy of further examination. In Chapter 3, the Schrödinger-Poisson system developed here is expanded to include the effects of other types of potentials on the halo, including the addition of a black hole and a distribution of visible matter.

CHAPTER 3

ADDITION OF EXTERNAL POTENTIALS

In the previous chapter, a simple model for a Schrödinger-Poisson system (hereafter referred to as the S/P system) was developed, and the fundamental ground state solution to that model was computed. The solution (hereafter referred to as the S/P only solution) has a form very similar to an Einasto profile with index $n \approx 0.56$, regardless of the physical parameters of the system. In particular, the mass of the particle and the mass and radius of the halo do not alter the shape of the solution, only its scale. Furthermore, these parameters are linked in such a way that, for a given particle mass, the radius of the halo actually decreases with increasing halo mass. This poses two problems which will now be addressed.

First, observations of real DM halos are well-described by Einasto profiles over a wide range of index values ($0.1 \lesssim n \lesssim 10$, e.g. Chemin et al. 2011). Larger halos tend to have more peaked inner slopes associated with larger indices ($n \geq 1$), while smaller galaxies are more like likely be 'cored,' having shallow inner slopes ($n < 1$). The S/P only solution is a cored density profile, suggesting it is most appropriate for a small galaxy. Since no external contributions to the potential have been considered so far, it may be best applied to LSB galaxies, where the dark matter content can be $\gtrsim 99\%$.

In addition, observed halos with larger mass tend to be larger in size, while the S/P only halo follows the reverse of this correlation. It is not surprising that a solution to the Schrödinger equation should behave this way. Increasing the halo mass in S/P system is equivalent to increasing the charge of the nucleus in a hydrogenic

atom or the size of the force constant in a harmonic oscillator. The latter cases are well known and result in more localized wave functions with higher central densities and smaller radii (Merzbacher 1997).

It is clear that the model presented in the previous chapter is insufficient to account for the variety of shapes and sizes observed in DM halos. One assumption that was made to simplify the model was to neglect the contributions of the baryonic matter content to the galactic potential. As a first step toward refining the model, two types of baryonic matter can be added to the system: the distribution of the galaxy's stellar content and the supermassive black hole presumed to occupy the galactic center.

3.1 The Central Supermassive Black Hole

Most massive galaxies are known to have a supermassive black hole at the center (Schödel et al. 2003; Ghez et al. 2003; Graham and Driver 2007). The potential created by a black hole can be modeled simply in the Schrödinger equation as a point source (like the nucleus of an atom). The interaction potential is thus

$$V(r) = -\frac{GmM_{BH}}{r}, \tag{3.1}$$

where M_{BH} is the mass of the black hole. This potential can be added directly to the Schrödinger equation,

$$E\psi = -\frac{\hbar^2}{2m}\nabla^2\psi + (V_{DM}(r) - \frac{GmM_{BH}}{r})\psi \ , \tag{3.2}$$

where $V_{DM}(r)$ is the Poisson potential Eq. (2.2) produced by the halo itself. As in Section 2.3, the system is now described by a set of coupled differential equations, (2.2) and (3.2).

The ground state solution for a Coulomb-like potential is an inverse exponential function in r, which corresponds to an Einasto profile with index $n = 1$. Such a profile

M_{Halo}	M_{BH}/M_{Halo}	ρ_0	$r_{1/2}$
10^{10}	0	7.61×10^{-6}	340.
	10^{-5}	7.61×10^{-6}	340.
	10^{-2}	8.58×10^{-6}	330.
	10^{-1}	1.99×10^{-5}	263.
	1	1.25×10^{-4}	172.
10^{11}	0	.0761	34.0
	10^{-5}	.0761	34.0
	10^{-2}	.0858	33.0
	10^{-1}	.199	26.3
	1	1.25	17.2
10^{12}	0	7.61×10^{2}	3.40
	10^{-5}	7.61×10^{2}	3.40
	10^{-2}	8.58×10^{2}	3.30
	10^{-1}	1.99×10^{3}	2.63
	1	1.25×10^{4}	.172

Table 3.1. Central mass densities and median radii for S/P halos with supermassive black holes and a particle mass of 10^{-24} eV. Columns from left to right: halo mass in 10^{12} solar masses; black hole mass ratio $\frac{M_{BH}}{M}$; central density in 10^8 solar masses/kpc^3; and median in kpc.

has a finite negative derivative at $r = 0$, giving it a slight cusp. The S/P only solution obtained in the previous chapter resembles an Einasto profile with $n \approx 0.56$, whose derivative is 0 at the core. A system containing both types of potentials can therefore be expected to land somewhere in between these profiles.

Figure 3.1 gives a sampling of solutions with different black hole-to-galaxy mass ratios $\frac{M_{BH}}{M}$, and it's clear that a more massive black hole produces a smaller, more concentrated dark matter halo. These plots are not unique to a specific halo mass. The condition connecting the physical parameters of the halo (Eq. 2.7) still holds even with the addition of a black hole, though the constant now depends only on the mass ratio $\frac{M_{BH}}{M}$. This relationship becomes clear when looking at the solutions under a range of different parameters. Table 3.1 lists the core density and median radii for

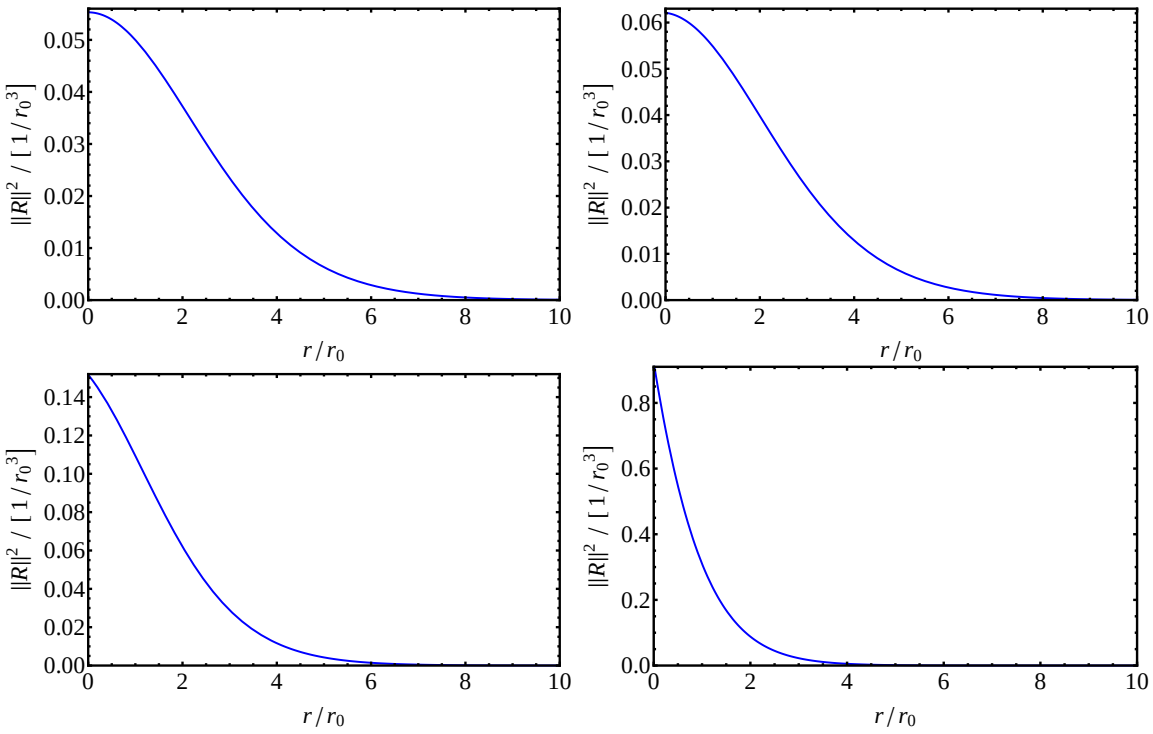

Figure 3.1. Density profiles for an S/P halo with black hole mass ratios $\frac{M_{BH}}{M}$ of 10^{-5} [upper left], 10^{-2} [upper right], 10^{-1} [lower left], and 1 [lower right] in terms of the scale radius r_0. These graphs are scale-independent, meaning they are applicable for any set of parameters satisfying Eq. 2.7. For a halo of 10^{11} solar masses, a particle mass of $10^{-}24$ eV, and a scale radius of 8.5 kpc, the density here is measured in units of $1.4 * 10^8$ solar masses/kpc^3.

various of halo and black hole masses. The difference in these values is small for halos more than a few orders of magnitude larger than their black holes.

Figure 3.2 permits a direct comparison between the halo densities. In the left panel, the densities are plotted to scale. For halos with $\frac{M_{BH}}{M}$ of 10^{-5} (orange) and 10^{-2} (red), the black hole produces only a small perturbation. For a galaxy with a black hole equal in mass to its halo (blue), the increase in density becomes apparent. In the right panel of Figure 3.2 the densities are plotted to a uniform height, allowing for a better comparison of shape. Bearing only a small black hole, the orange and red

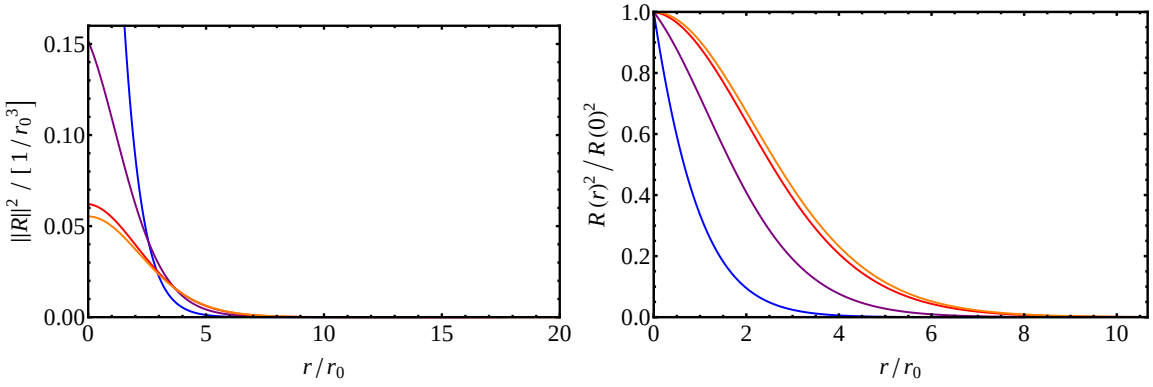

Figure 3.2. Comparison of the density profiles of a constant-mass S/P halo with black hole mass ratios $\frac{M_{BH}}{M}$ of 1 [blue], 10^{-1} [purple], 10^{-2} [red], and 10^{-5} [orange]. The left panel shows the normalized probability density of a single particle, with r given in terms of the arbitrary scale radius r_0. In the right panel these densities have been scaled to an initial value of 1 to emphasize the differences in the halo shapes. There is little difference between $\frac{M_{BH}}{M} = 10^{-2}$ and $\frac{M_{BH}}{M} = 10^{-5}$, reflecting the fact that at these ratios the black hole potential is dwarfed by that of the DM. The larger $\frac{M_{BH}}{M}$ becomes, the more the density resembles an electron in the ground state of the hydrogen atom.

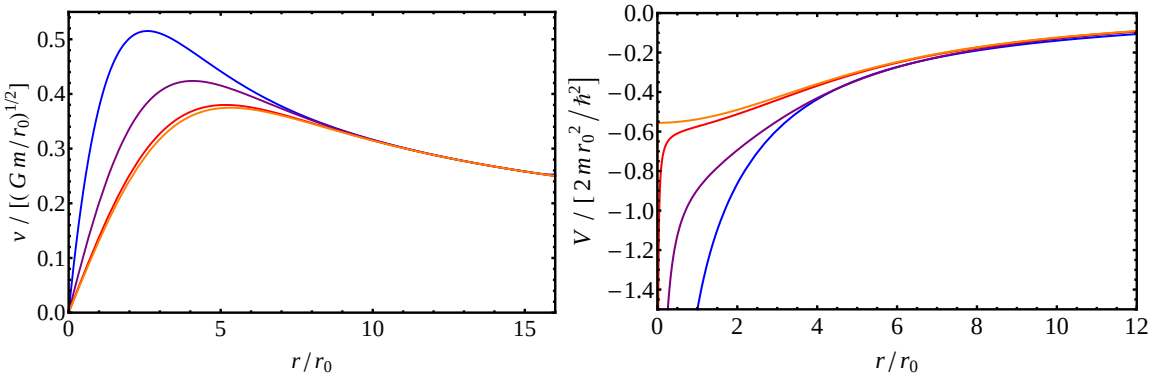

Figure 3.3. Comparison of the radial velocity curves [left panel] and the galactic potential [right panel] for a constant-mass S/P halo with black hole mass ratios $\frac{M_{BH}}{M}$ of 1 [blue], 10^{-1} [purple], 10^{-2} [red], and 10^{-5} [orange].

halos have a rounded shape and a flat cores. The blue halo is quite peaked, owing to the influence of the large point source potential in its center.

A comparison of the rotation curves and galactic potentials is given in Figure 3.3. The plots are scale-independent, meaning they hold for any fixed values of particle mass and halo mass. The left panel shows the radial velocity of an orbiting body within the host galaxy. The right panel shows the galactic potential. Moving from orange to blue, the effect of an increasing black hole mass is visible as a widening singularity at the origin. The shape of the potential in Figure 3.3 helps inform the shape of the density in Figure 3.2. A shallow, flat potential produces a rounded, flat wave function, while a singular potential produces a sharp, cuspy wave function.

There is a weak correlation between a galaxy's mass and the mass of the black hole at its core (Graham and Driver 2007). In general, larger galaxies are often host to more massive black holes, but the ratio between halo mass M and black hole mass M_{BH} varies greatly. Recent models have estimated the mass of the Milky Way to be $1.26 \pm 0.24 \times 10^{12}$ solar masses (McMillan 2011), and the black hole in its center has been measured at $4.1 \pm 0.6 \times 10^{6}$ solar masses (Ghez et al. 2008), giving $\frac{M_{BH}}{M} \approx 3.1 \times 10^{-5}$. The largest known black holes on record are in two elliptical galaxies, NGC 3842 and NGC 4889. McConnell et al. (2011) have estimated the masses of the black holes at the centers of these galaxies to be around 9.7×10^{9} solar masses and 2.1×10^{10} solar masses, respectively. The models provided in this study produce an average estimated galaxy mass of 8.1×10^{11} solar masses for NGC 3842, giving it a black hole-to-galaxy mass ratio of $\frac{M_{BH}}{M} \approx \frac{1}{83}$. NGC 4889's estimated mass of 1.6×10^{12} solar masses gives it a ratio of $\frac{M_{BH}}{M} \approx \frac{1}{75}$. Many dwarf galaxies, meanwhile, are thought to have no central black hole at all (Graham and Driver 2007).

It is apparent from Figures 3.1-3.3 that in order to significantly change the shape of the S/P halo, a large $\frac{M_{BH}}{M}$ is needed. At $\frac{M_{BH}}{M}$ in the range of NGC 3842 and NGC 4889, there is a small but noticeable change in the halo shape. For values of black hole mass approaching 10% of total halo mass, the profile does indeed begin to look more cuspy. When the black hole mass exceeds the halo mass, the wave function approaches an Einasto value of $n \approx 1$. In this extreme, the black hole potential greatly overshadows the contribution of the halo itself, and so the system resembles that of a hydrogenic atom on a galactic scale.

Clearly a black hole can have an effect on the overall halo shape. If the black hole strength were unconstrained, it could expand the family of S/P solutions to Einasto indices of $0.56 \lesssim n \lesssim 1$, but for known values of black hole and halo mass the effect is not dramatic enough to explain the differences in observed halo types.

3.2 Distributions of Luminous Matter

Stars comprise the majority of the visible matter content within galaxies (Kutner 2003). Most large spiral galaxies consist of a central galactic bulge of stars; a flat disc of stars, gas, and dust; and a roughly spherical halo of hot gas, old stars, globular clusters, and dark matter. Most of the luminous mass is contained within the disk and the bulge. Elliptical galaxies range in shape from nearly spherical to highly elongated and typically have little discernible structure and a comparatively sparse interstellar medium (Kormendy et al. 2009).

Like their dark matter halos, the stellar components of most spiral and elliptical galaxies are well-fit by an Einasto profile (van der Wel 2007). Large ellipticals often have stellar densities with Einasto indices in the range of $n \approx 4$, while many dwarf elliptical galaxies have an $n \approx 1$ distribution. The disk portion of spiral galaxies also typically have an $n \approx 1$ distribution (Sérsic 1963).

The gravitational potential created by a luminous matter (LM) distribution can be derived from the Poisson equation,

$$\nabla^2 V(\mathbf{r}) = 4\pi G \rho_{\mathrm{LM}} \ . \tag{3.3}$$

If the LM density is known, Eq. (3.3) can be solved beforehand and added directly to the Schrödinger equation. This method can be used to observe the effects of specific types of LM distributions on the DM halo. The potential for an spherical Einasto distribution with $n = 1$ is given by Eq. (2.6). Then the Schrödinger equation becomes

$$E\psi = -\frac{\hbar^2}{2m}\nabla^2\psi + \left[V_{DM}(r) + V_{LM}(r)\right]\psi \ , \tag{3.4}$$

and the system is described by solving Eqs. 2.2 and (3.4). The mass and median of the LM density are additional free parameters.

Figure 3.4 shows a sampling of the resulting DM density profiles. As with the plots from the previous section, the left panels show the normalized probability density of a single particle in terms of the arbitrary scale radius r_0; the right panels show the same densities scaled to an initial value of 1. The plots are divided into three rows based on the supplied DM fraction. The top row contains profiles for a galaxy with a typical DM content of 90%. Colors are used to distinguish LM distributions with different median values. Blue indicates an LM distribution with a median of 2 times the scale radius. This represents a galaxy where the stellar matter is more tightly packed around the galactic nucleus. It can be seen that the result of this configuration is a more concentrated DM halo, with a larger central density value. The yellow curve is for a stellar distribution with 32 times the scale radius, indicating that the stars spread more thinly and out to a larger distance. The effect is a more diffuse DM halo.

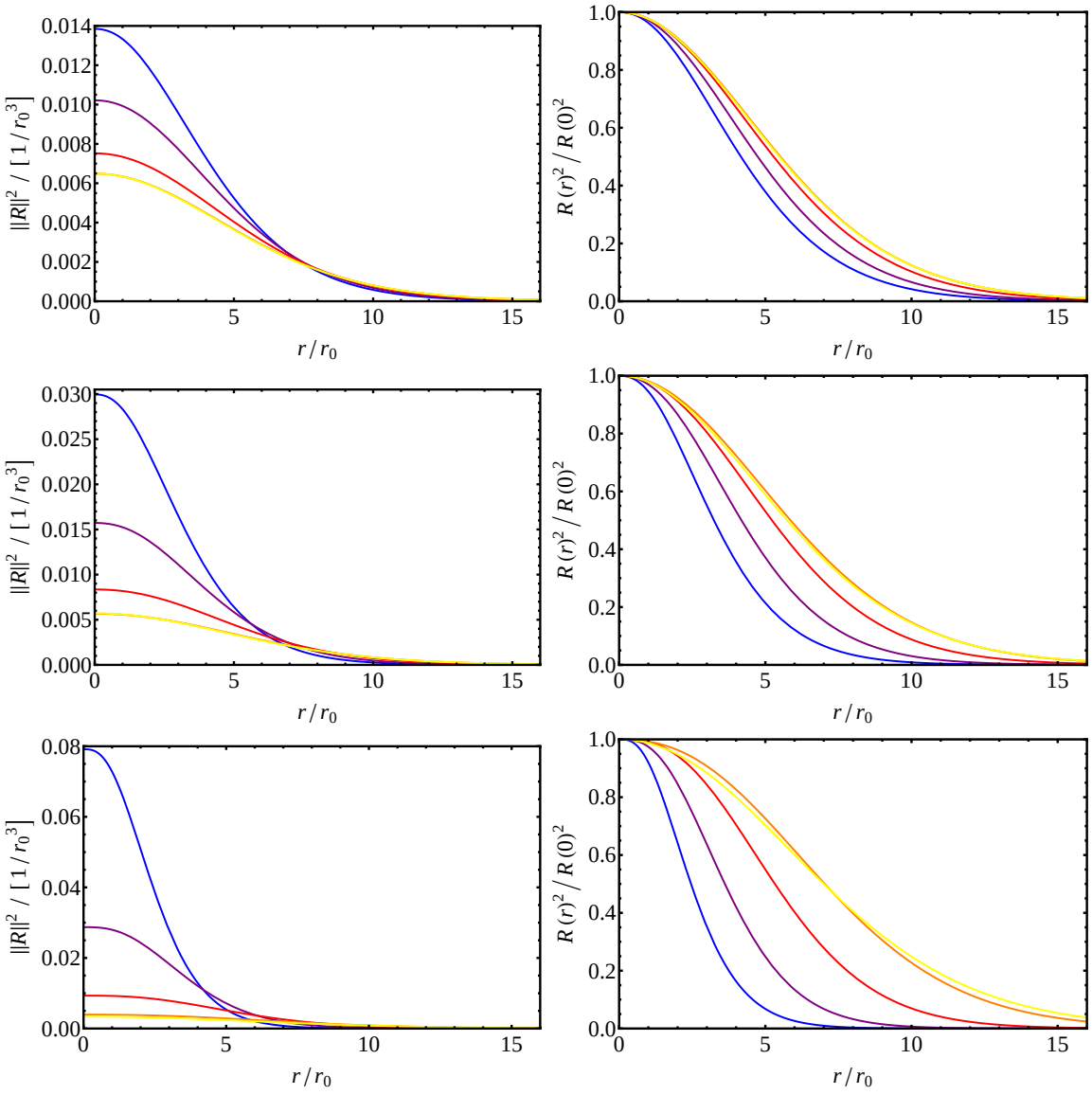

Figure 3.4. Comparison of the density profiles for an S/P halo with a galaxy mass-to-light ratio of 90% [top two panels], 75% [middle two panels], and 50% [bottom two panels], and a luminous Einasto $n = 1$ matter distribution with median of $2r_0$ [blue], $4r_0$ [purple], $8r_0$ [red], $16r_0$ [orange], and $32r_0$ [yellow]. The left panels show the normalized probability density of a single particle, with r given in terms of the arbitrary scale radius r_0. In the right panels these densities have been scaled to an initial value of 1 to emphasize the differences in the halo shapes.

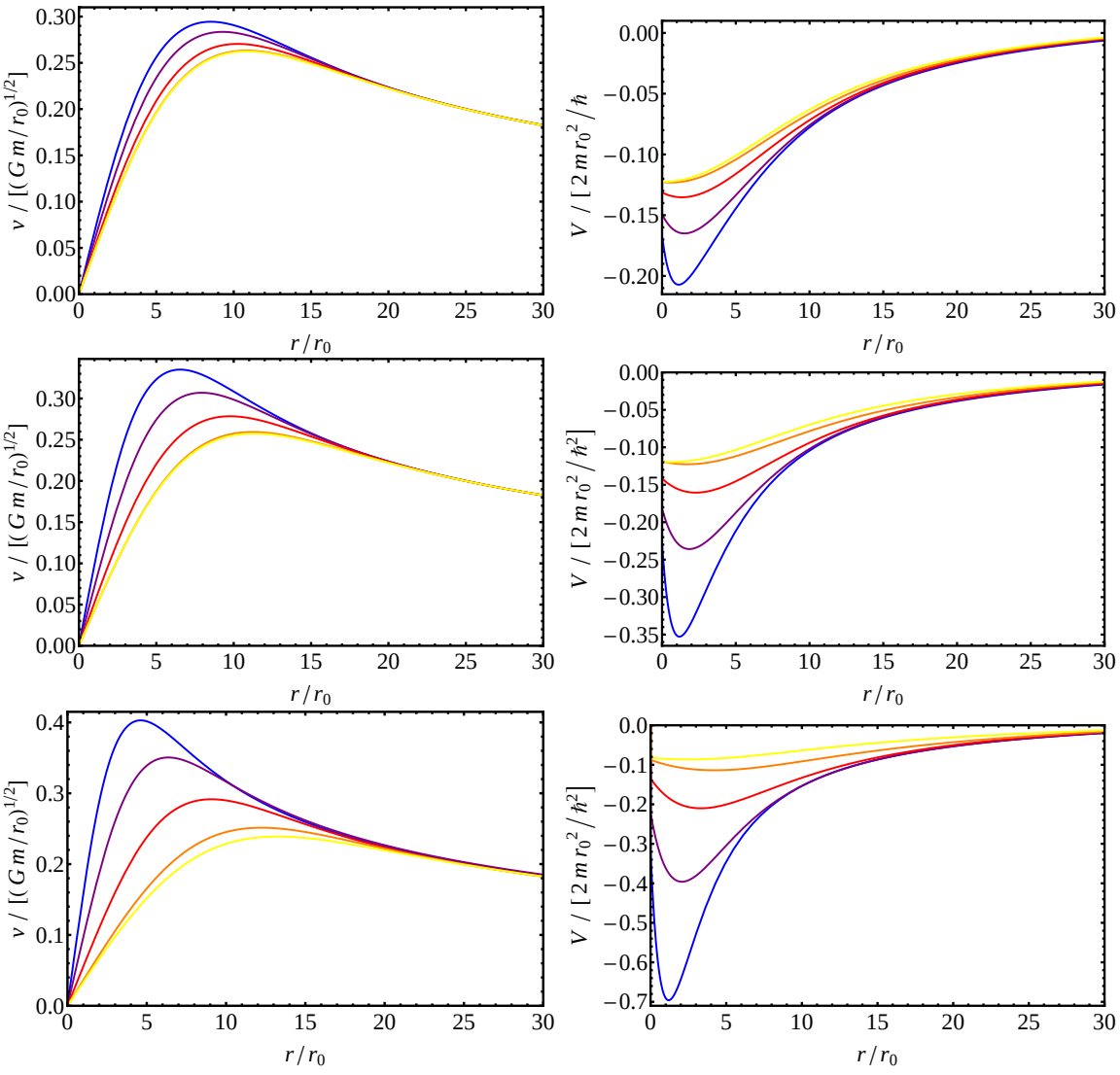

Figure 3.5. Comparison of the radial velocity curves [left panels] and the galactic potentials [right panels] for an S/P halo with a galaxy mass-to-light ratio of 90% [top two panels], 75% [middle two panels], and 50% [bottom two panels], and a luminous Einasto $n = 1$ matter distribution with median of $2r_0$ [blue], $4r_0$ [purple], $8r_0$ [red], $16r_0$ [orange], and $32r_0$ [yellow].

$DM\%$	$r_{1/2,(LM)}$	ρ_0	$r_{1/2,(DM)}$
90%	8.5	16.3	27.4
	17	12.1	29.7
	34	8.87	32.7
	68	7.65	34.5
	136	7.65	34.7
75%	8.5	35.3	21.0
	17	18.5	25.4
	34	9.85	31.1
	68	6.68	35.7
	136	6.74	36.1
50%	8.5	93.3	14.8
	17	33.9	20.3
	34	11.0	28.7
	68	4.64	38.6
	136	4.01	42.2

Table 3.2. Central mass densities and median radii for an S/P halo of 10^{11} solar masses with a luminous Einasto $n = 1$ matter distribution, assuming a particle mass of 10^{-24} eV. Columns from left to right: Galaxy DM fraction; median of the LM distribution in kpc; DM halo central density in 10^6 solar masses/kpc^3; and DM halo median in kpc.

The bottom panels show the DM profiles for a galaxy made of 50% DM and 50% LM. In such a galaxy the DM halo is more susceptible than usual to the effects of the LM. As before, the more compact LM distributions result in larger central DM halo densities, but the difference between LM median $2r_0$ and $32r_0$ is much more dramatic.

Table 3.2 shows the central mass densities and median radii for these cases given a DM halo of 10^{11} solar masses and a particle mass of 10^{-24} eV. These values can be compared to the $'100\%'$ DM halo case for a 10^{11} solar mass halo found in Table 3.1, where the core density is 7.61×10^6 solar masses and the median is 34.0 kpc. Unlike the black hole, which always has the effect of creating a tighter and sharper halo, the

LM distributions can either increase or decrease the DM halo size depending on their total mass and size.

For the 90% DM galaxy, a large and diffuse LM distribution increases both the median and the central mass density of the DM halo by a very small amount. For a more compact LM distribution at 8.5 kpc, the DM median is reduced by about 20% and ρ_0 is more than doubled.

In the 50% DM galaxy, the large LM distributions lengthen the DM halo considerably. This represents a greater share of the LM being located on the fringes of the galaxy, which tends to draw more of the DM away from its core. In the 8.5 kpc LM case, the DM median is reduced by more than half and ρ_0 is increased by an order of magnitude, similar to the case of a black hole.

In Accordance with Gauss's Law, the potential at a point outside of a distribution of matter with radius r is the same as it would be if all that matter were concentrated in a single point at the center. As the LM median becomes a smaller fraction of the halo median, more of the DM is located outside the LM region. For points outside the LM, the LM acts as a point source potential, drawing in the surrounding DM and lowering its median.

A galaxy with a black hole mass equal to its DM halo mass (see Table 3.1) can be seen as the limiting case of the 50% DM galaxy as the LM median approaches zero. The 8.5 kpc LM case produces a DM core density on the order of that produced by a black hole of the same mass. It also produces an even smaller median, which seems paradoxical. However, an examination of the halo shapes quickly explains this phenomenon. The black hole potential results in a halo with a cuspy shape much closer to an Einasto $n \approx 1$ profile. With the LM potential, the halo retains the flat, smooth core associated with a smaller Einasto index. When integrating to find the total mass of the halo over all space, the density is multiplied by r^2 to account for

the total area of the shell of radius r over which that mass is distributed. As a result, a cuspy density profile like Einsato $n \geq 1$ requires a larger volume to accommodate the same amount of mass than a smooth-cored density profile which approaches zero much more quickly (like Einsato $n < 1$). In other words, for a given halo mass, a cuspy profile will always have a larger median than a smooth-cored profile.

Figure 3.3 provides a comparison of the velocity curves and galactic potentials. As before, the plots are scale-independent. As expected, the radial velocity curves depicted in the left panels show a greater divergence for a lower DM fraction. The right panels show the interesting effects of the LM on the galactic potential. The first obvious change is the appearance of potential well displaced from the origin. The smaller values of LM median produce deeper wells closer to the origin, suggesting there is a correlation between the LM median and the minimum potential. For galaxies with smaller DM fractions, the wells are much more pronounced as a function of LM median, while in the galaxies with 90% DM and large LM medians there is no visible well at all. These wells have the effect of drawing more DM to the core of the halo, but because they occur away from the origin, they don't result in the cuspy cores associated with black holes.

Overall, the DM distributions don't show a large variance from the S/P only halo. As with the black hole, the most noticeable difference occurs when the LM mass approaches the DM mass, or when the galaxy's mass-to-light ratio approaches half. Even then, the radius of the LM distribution must be significantly smaller than that of the DM halo in order to have much effect. The black hole produces a steeper inner slope in the DM distribution precisely because all of its mass is at the core. An LM distribution spread out over a larger area produces a more gently sloping potential, damping its overall impact on the DM halo shape.

The stellar mass distribution is an important part of the DM picture, most notably because of the reliance on rotation curve data for constraining DM profiles. Any complete picture of the galactic potential must certainly include contributions from the LM, but its effect in many cases is small enough to ignore in a first-order calculation. Where is stands to have the most effect is in those galaxies with the lowest mass-to-light ratios.

3.3 The Gross-Pitaevskii Equation

Under the assumption that the interaction between a pair of DM particles is extremely weak, analysis in this dissertation has thus far been limited to finding solutions to a gravitational Schrödinger-Poisson system using the Hartree approximation and neglecting many-body effects. Because the particles are assumed to be bosons, there is no Pauli exclusion principle to restrict the number of particles allowed in each state.

The distribution of quantum states in a system of indistinguishable bosons in thermal equilibrium is governed by Bose-Einstein statistics, where the expected number of particles in each energy state is given by

$$n_i = \frac{d_i}{e^{\frac{(\epsilon_i - \mu)}{k_b T}} - 1} \ , \tag{3.5}$$

where d_i and ϵ_i are the degeneracy and the energy, respectively, of the i^{th} state; μ is the chemical potential; T is the absolute temperature; and k_b is the Boltzmann constant (Merzbacher 1997). Most of these quantities are unknown, but in the limit that $T \to 0$, all of the particles will collapse into the lowest energy state. In this sense, the model presented in Chapter 2 can be thought of as the $T \to 0$ approximation of the gravitational Schrödinger-Poisson system. A more detailed analysis of the implications of Eq. (3.5) is provided in Chapter 4.

A gas of weakly interacting bosons cooled to temperatures near absolute zero is known as a Bose-Einstein Condensate (BEC) (Pathria 1996). Because all or nearly all of the particles in a BEC are in the ground state, they can be described by the same wave function. This means that quantum effects become visible on a macroscopic scale. BECs have been vigorously researched since their discovery. The first man-made BEC was created in 1995 using rubidium-87 atoms (Anderson et al. 1995). Since then, BECs have been made from sodium-23 (Davis et al. 1995) and lithium-7 (Bradley et al. 1995), among others. BECs have even been observed in photons (Klaers et al 2010).

The governing equation used to describe a BEC is the Gross-Pitaevskii equation,

$$\mu\psi = -\frac{\hbar^2}{2m}\nabla^2\psi + \left[V(r) + g|\psi|^2\right]\psi \ , \tag{3.6}$$

where $V(r)$ is an external potential; $g = \frac{4\pi\hbar^2 a_s}{m}$ is the coupling constant; and a_s is the scattering length (Pitaevskii and Stringari 2004). ψ is the single particle wave function, and

$$\int_{-\infty}^{\infty} \psi^*\psi \ dV = N \ , \tag{3.7}$$

where N is the total number of particles.

The Gross-Pitaevskii equation is simply the Schrödinger equation with a non-linear scattering term $g|\psi|^2$ added to the potential. The scattering length a_s is interpreted to be the distance at which the fine structure of the interaction potential becomes important. To take a classical example, the scattering length of a billiard ball is simply the radius of the ball. For more complex potentials, the scattering length is often found empirically. In the limit that $a_s \to 0$ the scattering term disappears and the Schrödinger equation is recovered.

Since the primary dark matter model considered in this dissertation consists of bosons condensed to the same ground state, it could easily be interpreted as a BEC.

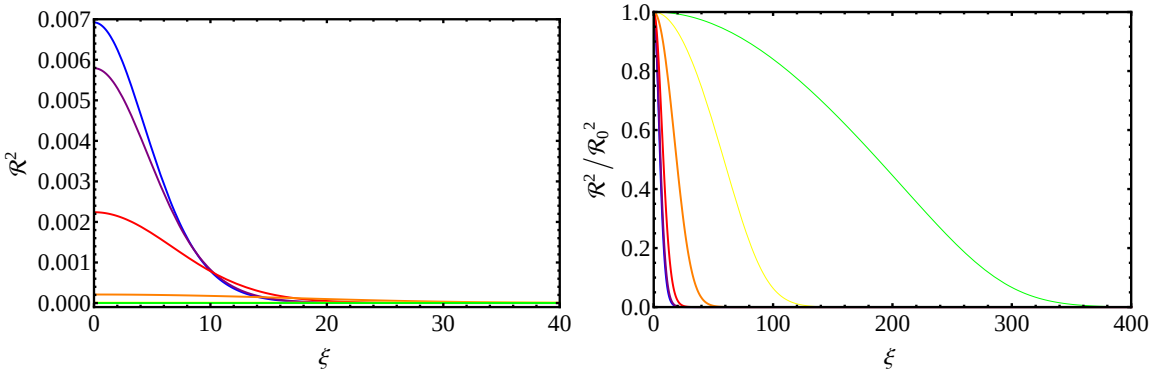

Figure 3.6. Comparison of the density profiles of an S/P halo with $\mathcal{B} = 1$ and $\mathcal{C} = 0$ [blue]; 1 [purple]; 10 [red]; 10^2 [orange]; 10^3 [yellow]; and 10^4 [green]. The left panel shows the normalized probability density of a single particle. In the right panel the densities have been scaled to an initial value of 1 to emphasize the differences in the halo shapes.

It is reasonable to consider, then, whether there is any scattering between particles and how such behavior might affect the halo structure. If the potential $V(r)$ in Eq. (3.7) is taken to be the dark matter Poisson potential from Eq. (2.2), then the Gross-Pitaevskii equation can be used in place of the Schrödinger equation to form an S/P system with an added potential term. This system of equations is doubly nonlinear; both the repulsive scattering term and the Laplacian of the attractive Poisson potential are proportional to ψ^2.

The scattering length a_s serves as an additional free parameter. In order to compare the relative strengths of the S/P potential and the new scattering term, it will be helpful to rewrite the equations entirely in terms of dimensionless variables. Let $\xi = r/r_0$ be the measure of distance, where r_0 is an arbitrary scaling parameter, and let the dependent variables be $\mathcal{R}(\xi) = (\frac{m{r_0}^3}{M})\, R(\xi)$ and $\mathcal{V}_{\mathcal{DM}}(\xi) = (\frac{2m{r_0}^2}{\hbar^2})\, V_{DM}(\xi)$. Then Eqs. (3.7), (2.2), and (3.8) become

$$\nabla^2 \mathcal{R}(\xi) = \left[\mathcal{B}\ \mathcal{V}(\xi) + \mathcal{C}\ \mathcal{R}(\xi)^2 - \mathcal{D}\right] \mathcal{R}(\xi)\ , \tag{3.8}$$

$$\nabla^2 \mathcal{V}_{\mathcal{DM}}(\xi) = \mathcal{R}(\xi)^2\ ,\ \textit{and} \tag{3.9}$$

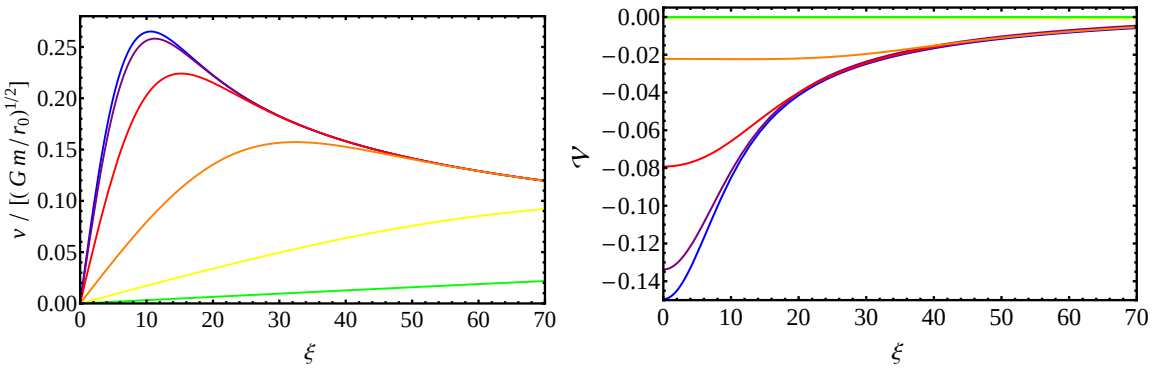

Figure 3.7. Comparison of the radial velocity curves (left panel) and the galactic potential (right panel) for a an S/P halo with $\mathcal{B} = 1$ and $\mathcal{C} = 0$ [blue]; 1 [purple]; 10 [red]; 10^2 [orange]; 10^3 [yellow]; and 10^4 [green].

$$\int_0^\infty \xi^2 \, \mathcal{R}(\xi)^2 \, d\xi = 1 \ , \tag{3.10}$$

respectively, where $\mathcal{B} = \frac{2G}{\hbar^2} m^2 M r_0$ and $\mathcal{C} = \frac{2a_s}{m r_0} M$ (referred to hereafter as the Poisson and scattering parameters, respectively) determine the relative strengths of the potential terms, and $\mathcal{D} = \frac{2m{r_0}^2}{\hbar^2}\mu$ is the energy parameter.

Figure 3.4 gives the ground state densities for $\mathcal{B} = 1$ over a range of $\mathcal{C}$ values. The standard S/P only solution is recovered in the case of $\mathcal{C} = 0$ [blue]. The most noticeable effect of the added scattering term is spread of the distributions. In the case of $\mathcal{C} = 10^5$, the halo is stretched by more than an order of magnitude, and its shape is significantly altered. The other smooth-cored profiles encountered so far have a distinct rounded inner section with negative second derivative. This is sometimes referred to as the 'core' of a density profile (not to be confused with the 'core density,' which is the density at $r = 0$). Outside this core, the second derivative is positive, and the density decays to zero as $r \to \infty$. For the $\mathcal{C} = 10^5$ case, the 'core' takes up almost the entire halo, causing it to resemble a bubble or spheroid.

One of the consequences of the sizeable cores produced in halos with large $\mathcal{C}$ is shown in the galaxy's rotation curves (Figure 3.7, left panel). The larger core

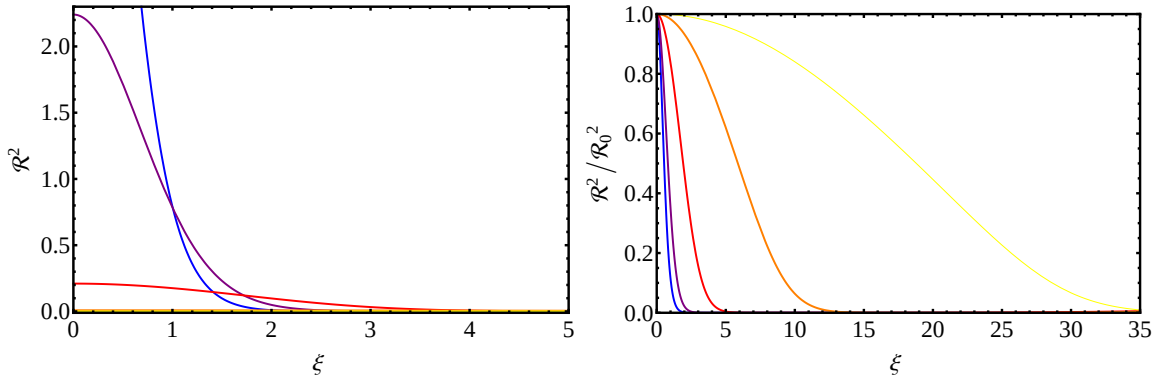

Figure 3.8. Comparison of the density profiles of an S/P halo with $\mathcal{B} = 10$ and $\mathcal{C} =$ 0 [blue]; 1 [purple]; 10 [red]; 10^2 [orange]; and 10^3 [yellow]. The left panel shows the normalized probability density of a single particle. In the right panel the densities have been scaled to an initial value of 1 to emphasize the differences in the halo shapes.

causes the velocity curve to increase over a longer range. The potential for these halos (Figure 3.7, right panel) is also much shallower.

Figures 3.8 and 3.9 show the same details as Figures 3.6 and 3.7 for $\mathcal{B} = 10$. The central mass density and median halo values are provided in Table 3.3. As noted in the graphs, the largest $\mathcal{C}$ values increase the halo median by more than order of magnitude while lowering the central density by several orders.

Since the scattering term in the potential is repulsive, it serves to spread out the distribution rather than concentrating it. Its proportionality to the density prevents too much occupation of a given region of space. As a result, there is an upper limit on the value of $\mathcal{C}$ in order for a bound state to be possible. Analyzing the results for $\mathcal{B}$ values ranging from 10^{-4} to 10^3, the upper limit for a bound state is on the order of $\mathcal{B}\,\mathcal{C} \sim 10^5$. Since the product of $\mathcal{B}$ and $\mathcal{C}$ is $\frac{4G}{\hbar^2 a_s m M^2}$, this formula can be used to find the upper bound on the scattering length a_s. Taking a typical large galaxy halo mass of 10^{12} solar masses and a particle mass of 10^{-24} eV, this gives an upper bound

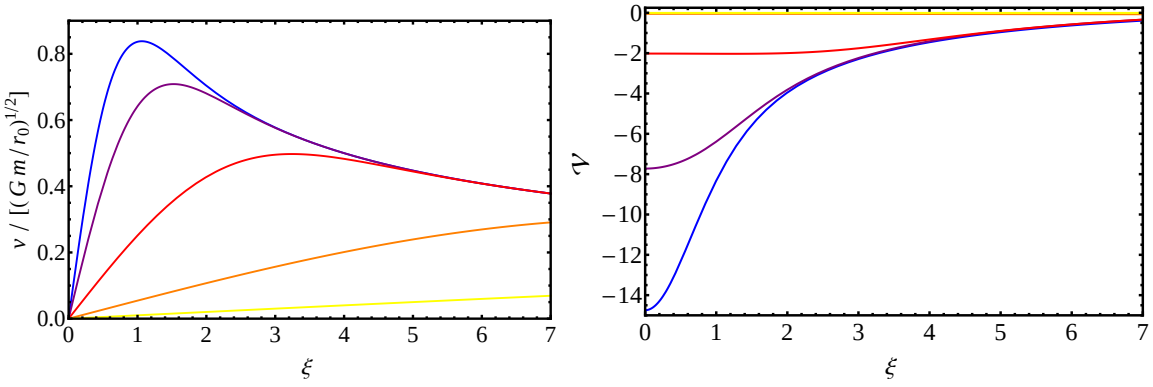

Figure 3.9. Comparison of the radial velocity curves (left panel) and the galactic potential (right panel) for a an S/P halo with $\mathcal{B} = 10$ and $\mathcal{C} = 0$ [blue]; 1 [purple]; 10 [red]; 10^2 [orange]; and 10^3 [yellow].

on the scattering length of around $5.8 \times 10^{-89} m$, or 54 orders of magnitude lower than the Planck length.

Since the Planck length is the lower limit of distance measurement in quantum mechanics, this result can't be taken as physical. There are several possible interpretations. The simplest is that DM particles of this nature have no scattering properties. If they do scatter, it may be that the Gross-Pitaevskii equation does not apply to them. If it does apply to them, it may mean that the scattering term requires a different interpretation than the one assumed for typical Bose-Einstein condensates.

Though the Pauli Exclusion principle does not apply to bosons, other exclusionary principles do exist in nature. General Relativity places an upper limit on the amount of mass that can be contained within a given volume defined by the Schwarzschild radius (Cheng 2010). Since the Compton wavelength for these particles has an astronomical scale and the wave functions are heavily overlapping, there is a small but ever-present probability of a handful of particles being localized to within a radius smaller than the what the Schwarzschild limit would allow. Any mechanism which would act to prevent these particle from simultaneously being in a given region

$\mathcal{B}$	$\mathcal{C}$	ρ_0	$r_{1/2}$
1	0	7.61	34.0
	1	6.37	35.9
	10	2.47	48.2
	10^2	.231	101.
	10^3	9.89×10^{-3}	278.
	10^4	3.39×10^{-4}	840.
10	0	7.61×10^4	3.40
	1	2.46×10^4	4.82
	10	2.31×10^3	10.1
	10^2	98.9	27.8
	10^3	3.39	84.0

Table 3.3. Central mass densities and median radii for an S/P halo of $\mathcal{B} \times 10^{11}$ solar masses and a Gross-Pitaevskii scattering term $\mathcal{C}$, assuming a particle mass of 10^{-24} eV. Columns from left to right: Poisson parameter $\mathcal{B}$; scattering parameter $\mathcal{C}$; DM halo central density in 10^6 solar masses/kpc^3; and DM halo median in kpc.

would constitute a type of exclusion, and would result in a scattering of particles. Currently there is no commonly accepted theory which unifies General Relativity and quantum mechanics, and the exact nature of this hypothetical scattering and its computational form are beyond the scope of this dissertation.

Like the other modifications to the potential, a Gross-Pitaevskii scattering term alone is not enough to incorporate all observed DM halo types into the same model, but its inclusion does widen the spectrum of possible halo shapes and behaviors.

3.3.1 Addition of a Black Hole

In this section the effects of the repulsive Gross-Pitaevskii nonlinearity and the attractive black hole singularity are studied in combination by inserting a black hole potential into Eq. (3.8).

Figure 3.10 gives the ground state densities for a halo with $\mathcal{B} = 1$ and $\mathcal{C} = 10000$ and black holes of three different mass ratios $\frac{M_{BH}}{M}$; Figure 3.11 shows the radial

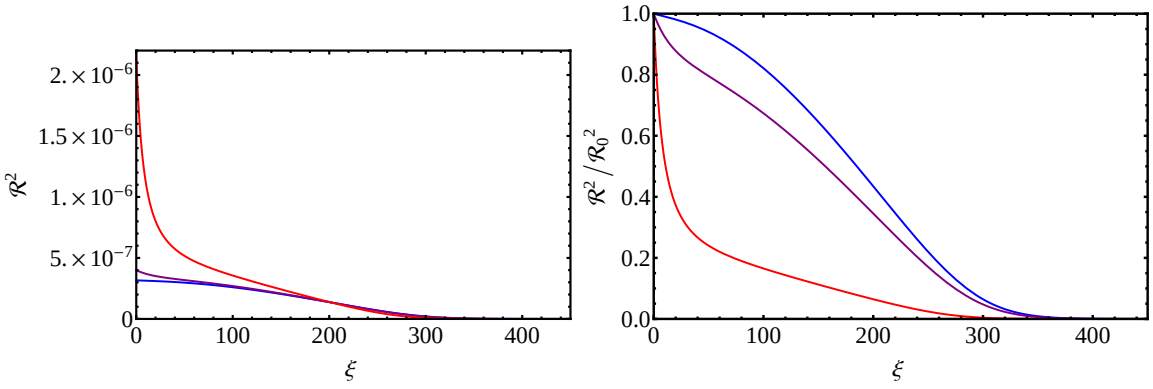

Figure 3.10. Comparison of the density profiles of an S/P halo with $\mathcal{B} = 1$, $\mathcal{C} = 10000$, and black hole mass ratios $\frac{M_{BH}}{M}$ of 10^{-3} [blue], 10^{-2} [purple], 10^{-1} [red]. The left panel shows the normalized probability density of a single particle. In the right panel the densities have been scaled to an initial value of 1 to emphasize the differences in the halo shapes.

velocity curves and potential wells. This trio of unusual shapes has several noteworthy qualities. For $\frac{M_{BH}}{M} = 10^{-3}$ [blue], the halo is mostly unchanged from the no-black hole case. For $\frac{M_{BH}}{M} = 10^{-2}$ [purple], the density very near the origin is cuspy and linear. A noticeable hump occurs not far from the origin, and thereafter the halo takes on the rounded shape and negative second derivative associated with the previous $\mathcal{C} = 10000$ halos. For $\frac{M_{BH}}{M} = 10^{-1}$ [red], there is a pronounced cusp at the origin followed by a sharp bend. The second derivative stays positive, a characteristic shared with Einasto profiles $n \geq 1$. Strangely, this curve is well approximated by an Einasto profile with $n = 2$ out to arounf $\xi \sim 150$. Thereafter the density continues on an almost linear path before entering exponential decay. The Einasto $n = 2$ function decays as the exponential of the square root of r, meaning it takes longer than an ordinary exponential function to approach zero.

This behavior appears to be even more pronounced for higher black hole mass ratios and for higher values of $\mathcal{C}$. In both cases, however, the halo is so loosely bound that a ground state is difficult to find within the normal limits of numerical precision.

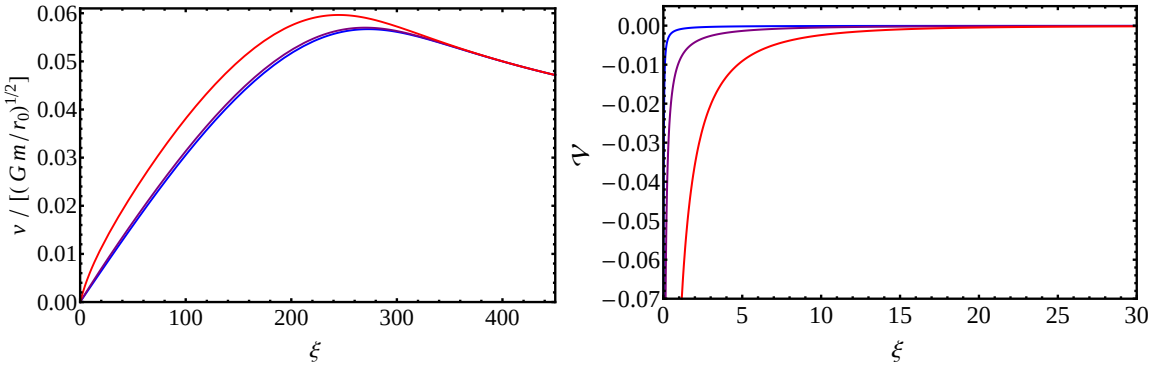

Figure 3.11. Comparison of the radial velocity curves (left panel) and the galactic potential (right panel) for a an S/P halo with $\mathcal{B} = 1$, $\mathcal{C} = 10000$, and black hole mass ratios $\frac{M_{BH}}{M}$ of 10^{-3} [blue], 10^{-2} [purple], 10^{-1} [red].

Determining what if any bound states can occur at these extreme values will require a high degree of precision and computing power, and it is left as an avenue for future study.

3.4 Summary

Stable ground state solutions to the Schrödinger-Poisson system with additional potentials were computed and their properties compared to known halo types.

The addition of a black hole to the S/P system provided a more peaked distribution associated with simulated DM halos and with observed halos in large galaxies. The black hole also had the effect of drawing the mass of the halo inward, creating a larger core density and smaller median. The galactic rotation curve achieved a higher maximum at a closer radius than the no-black hole case, while the galactic potential gained a singularity that began to dominate the halo at small radii. The effects of the black hole were most noticeable when its mass was within an order of magnitude of the halo mass.

Adding a luminous matter distribution preserved the smooth-cored profile of the S/P only solution. LM distributions with smaller radii had the effect of drawing the mass in toward the core, while large-radius LM profiles actually pulled mass away from the core, spreading out the halo. The galactic rotation curve achieved its sharpest peak when the LM had the smallest radius and a mass comparable to the DM. The galactic potentials gained a visible well, with smaller values of LM median producing deeper wells closer to the origin, suppressing the appearance of a cusp.

A Gross-Pitaevskii scattering term created a rounder halo, with the strongest terms resulting in an almost parabolic appearance. The halos were spread out over a larger area, with smaller core densities. The addition of a black hole created some unusual halo shapes, and for certain values began to emulate the properties of Einasto profiles with $n > 1$.

Each added potential expanded the gravitational S/P model to incorporate a larger range of DM halo types, creating both cuspy and smooth-cored profiles as well as extending the possible range of central density and median radius values permitted. Tables 3.1 - 3.3 demonstrate how a large variation can occur in these parameters even when the particle mass is held constant. This is in contrast to the S/P only model, where the halo parameters were limited in scope by Eq. (2.7). Chapter 4 will examine the possibility of incorporating excited states into the model as a means of further expanding its range.

CHAPTER 4

INCLUSION OF EXCITED STATES

All the QDM models considered in this dissertation and the references therein have assumed that the particles are bosons. If a DM halo on the order of $10^6 \sim 10^{13}$ solar masses is to be made up of particles on the order of 10^{-24} eV, then the population of the halo can reach or exceed 10^{100} particles.

If one considers for reference that the hydrogen atom permits a total of $2n^2$ electrons per energy state n (Merzbacher 1997), a quick calculation shows that even just 10^{18} particles will require more than 10^6 excited states. It's easy to imagine that a system of 10^{100} fermions would require an extreme and unprecedented number of energy levels. By contrast, the largest atoms contain fewer than 120 electrons, requiring at most 5 or 6 energy levels. Even these are notoriously complex and difficult to model. It's safe to say that no existing computer could model a system of 10^{100} fermions.

Of course, if one started with the assumption that the particles were fermions, the range of masses approximated in such a model would be different. A higher particle mass would mean fewer particles required to make up the halo, and subsequently fewer excited states to be considered. However, raising the mass by more than a few orders of magnitude lowers the Compton wavelength to significantly below the parsec scale while still requiring an enormous particle population. This makes a fermionic QDM model an unlikely prospect.

Even for bosons, it's sensible to consider the implications of DM halos with excited states. For the low temperatures assumed in a BEC, the realistic assumption

is that most of the particles are in the ground state. However, in any real-world application, with T never quite reaching absolute zero, there will always be some percentage of occupied excited states (Pathria 1996).

The occupation numbers for the energy states of a bosonic system was given by Eq. (3.5). The equation depends in part on temperature, and a typical BEC will have nearly all its particles in the ground state with a handful in the first excited state. If this idea is extended to the QDM model, a problem quickly arises. The wave function used in the Schrödinger and Poisson equations described a particle in a single state. If multiple states are considered within the same halo, then both states will contribute to the overall potential. This potential will be different from the one that would occur if all the particles were in the ground state. In moving from the ground state to the first excited state, the particles have changed the very potential in which they were bound. In addition, both the ground and excited states must satisfy the overall potential they create. This requires solving an extra Schrödinger equation for the excited state.

Adding even a small percentage of excited particles seems to have magnified the nonlinearity of the S/P system. In order to establish how this problem might be approached, the next few sections will proceed in steps of increasing complexity, beginning with simplifying assumptions and extrapolating the results to acquire actual solutions.

4.1 Single-State Halos

Before considering the full complexities of a mixed state halo, it is instructive to begin with the case of a halo where all the particles are in the same excited state. Solutions of this nature are found readily from the models considered in the previous chapters. Those sections sought ground state solutions by selecting only those wave

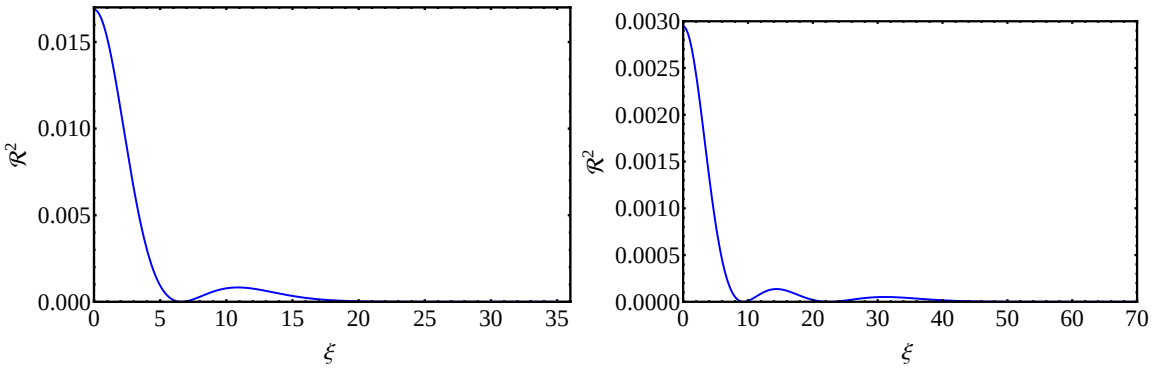

Figure 4.1. Density profiles for an S/P halo in the 1st excited state [left panel] and second excited state [right panel].

functions that were nodeless. To find the excited states, one merely has to change the energy until a state with nodes is found.

Figure 4.1 shows the density profiles for two such solutions, namely an S/P halo entirely in the first (left panel) and second (right panel) excited states. They are similar in appearance to excited states of the hydrogen atom but with a flat core instead of a cuspy one.

The fine structure is apparent in the halo potentials (Figure 4.2), having the same basic shape as the ground state S/P solution but with a characteristic bump associated with each node. The rotation curves plotted in Figure 4.2 have an even more dramatic character, producing visible wavelike deviations from the ground state case. Interestingly, many real galactic rotation curves also exhibit this clear wavelike form (Karachentsev and Xu 1991; Wozniak and Pfenniger 1996).

The possibility of an entire halo in an excited state would seem to violate the conditions of Bose-Einstein statistics. However, for a nonlinear problem the question of energy level occupation becomes more complicated. This question is examined in Section 4.3.

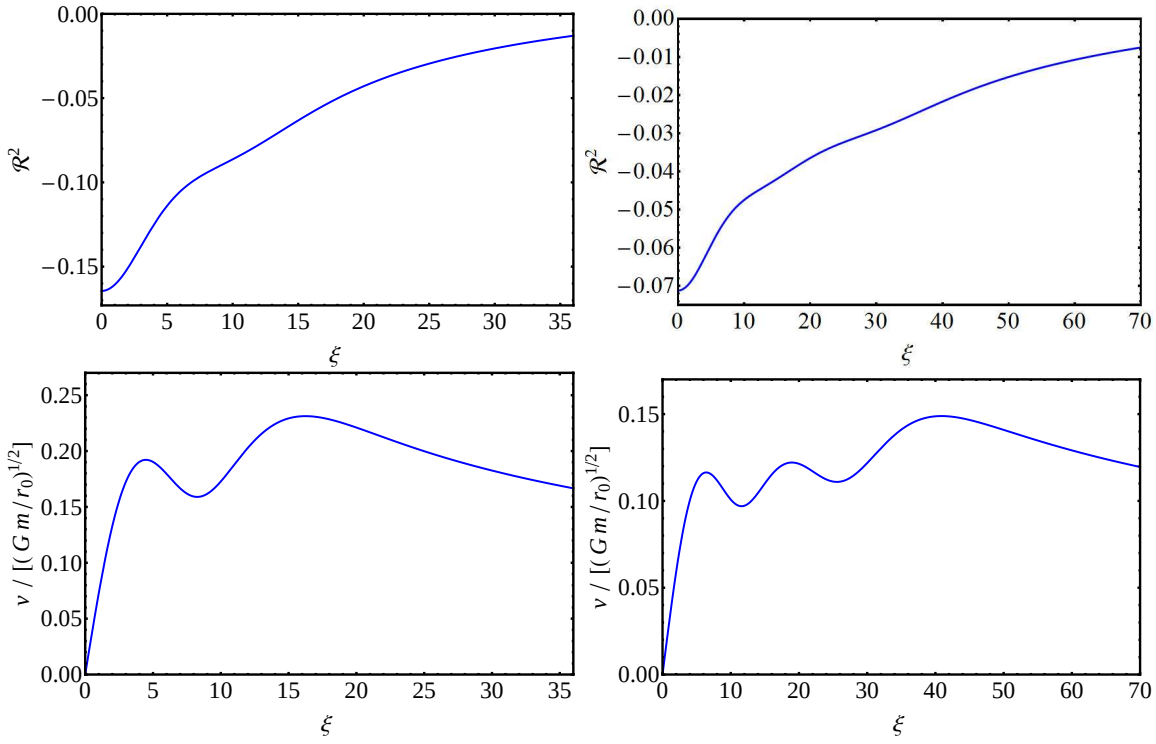

Figure 4.2. Galactic potentials for an S/P halo in the 1st excited state [upper left panel] and second excited state [upper right panel]; galactic rotation curves for an S/P halo in the 1st excited state [lower left panel] and second excited state [lower right panel].

4.2 Mixed-State Halos

If the particles are permitted to be in a mix of more than one state, it is necessary to bring multiple Schrödinger equations into the picture. For a halo with two different eigenstates, the S/P system contains three equations. A two-state halo can be treated as two separate halos occupying the same space, each contributing to the overall potential. Each wave function must satisfy the Schrödinger equation with the same potential and a different energy. Using the dimensionless variables defined in chapter 3,

$$\nabla^2 \mathcal{R}_i(\xi) = [\mathcal{B}\ \mathcal{V}(\xi) - \mathcal{D}_i]\, \mathcal{R}_i(\xi) \quad \textit{and} \tag{4.1}$$

$$\nabla^2 \mathcal{R}_j(\xi) = [\mathcal{B}\ \mathcal{V}(\xi) - \mathcal{D}_j]\, \mathcal{R}_j(\xi)\ , \tag{4.2}$$

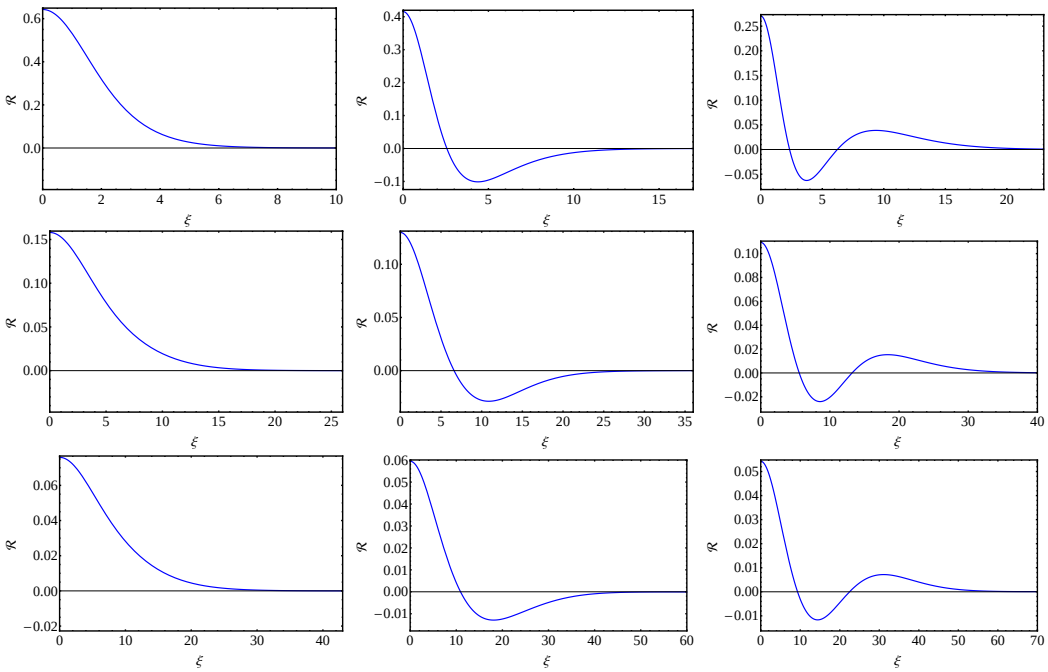

Figure 4.3. Wave functions for a single particle with state $n = 1$ [left column], 2 [middle column], and 3 [right column], embedded in a parent halo of state $N = 1$ [top row], 2 [middle row], and 3 [bottom row].

where $\mathcal{R}_i(\xi)$ and $\mathcal{R}_j(\xi)$ are the single particle radial wave functions of the two individual eigenstates, and $\mathcal{D}_i$ and $\mathcal{D}_j$ are their respective energy eigenvalues. The potential given by the Poisson equation, which now depends on both densities, is

$$\nabla^2 \mathcal{V}(\xi) = c_i \mathcal{R}_i(\xi)^2 + c_j \mathcal{R}_j(\xi)^2 \ . \tag{4.3}$$

where c_i and c_j represent the fractions of particles in each of those states, and $c_i + c_j = 1$. In addition, each particle must satisfy its own normalization condition,

$$\int_0^\infty \xi^2 \ \mathcal{R}_i(\xi)^2 \ d\xi = 1 \quad \textit{and} \quad \int_0^\infty \xi^2 \ \mathcal{R}_j(\xi)^2 \ d\xi = 1 \ . \tag{4.4}$$

The usual numerical methods can be used to find ground or excited states, only now the problem contains six initial conditions to specify, ($\mathcal{R}_i(0)$, $\mathcal{R}_i'(0)$, $\mathcal{R}_j(0)$, $\mathcal{R}_j'(0)$, $\mathcal{V}(0)$, and $\mathcal{V}'(0)$), as well as the two energy eigenvalues. In effect the separate states

	$n=1$	$n=2$	$n=3$			$n=1$	$n=2$	$n=3$
$N=1$	.4130	.1726	.07374		$N=1$	2.008	5.374	10.44
$N=2$	.02497	.01688	.01197		$N=2$	5.296	12.05	18.94
$N=3$	.005764	.003539	.002945		$N=3$	8.713	20.64	31.16

Table 4.1. ${\mathcal{R}_0}^2$ [left] and $\xi_{1/2}$ [right] for the solutions in Figure 4.3

together form a nonlinear 2-body problem, making numerical solutions a challenge. With so many unknowns, it is difficult to know where to start.

It will be helpful to narrow down the range of possible initial conditions. Fortunately, the problem is simpler to solve in some limiting cases. One approach is put the entire halo into a single state N, and then add a single particle with state n. Since the second eigenstate contains only a single particle, its contribution to the potential can be neglected. This breaks the problem into two much simpler steps. First, the S/P system for the single-state N halo can be solved as in the previous section. Next, the potential resulting from that solution can be used in a separate Schrödinger equation, and a solution can be sought with the desired number of nodes specified by n.

Figure 4.3 shows the resulting single-particle wave functions when the first three states are considered. On the top row are the first three states (from left to right, $n = 1, 2$, and 3) for a single particle embedded in a halo entirely in the ground state ($N = 1$). The middle row shows the first three states for a particle in a halo entirely in the first excited state ($N = 2$), and the bottom row corresponds to a halo in $N = 3$. The result is a 3×3 grid of single-particle wave functions, and the diagonal corresponds to the cases where $N = n$.

Moving down across the grid, the individual states show almost no change in shape. Their scale, on the other hand, increases according to the scale of the parent

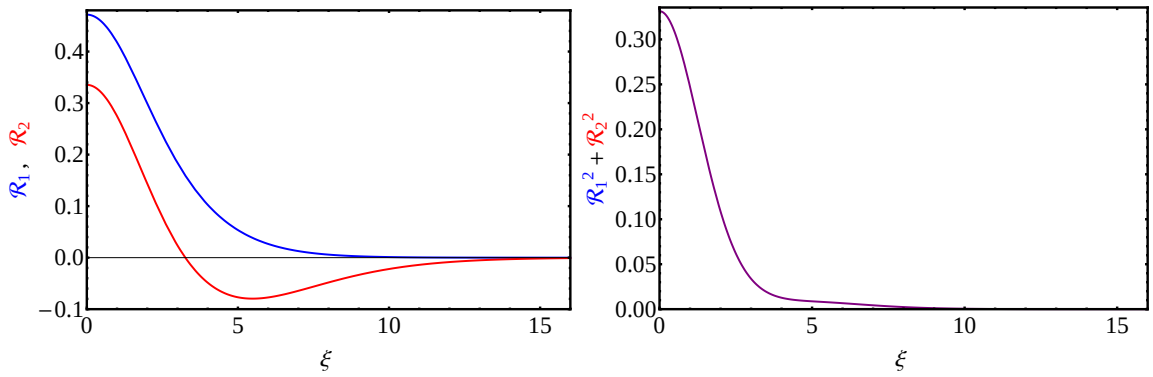

Figure 4.4. [Left panel]: Wave functions for a particle in a halo half in the ground state [blue] and half in the first excited state [red]. [Right panel]: The combined halo density function.

halo. From Figure 4.1 it is apparent central density has decreased from the first to the second excited state, while the effective radius has increased. These changes are reflected in Fig. 4.3, where the single-particle states have lower central densities (and higher effective radii) when embedded in halos of higher states. Likewise, a particle in the first excited state has a much higher central density when it is embedded in an $N = 1$ halo than when it's part of an $N = 2$ halo.

Table 4.1 gives the values of ${\mathcal{R}_0}^2$ and median $\xi_{1/2}$. This table can be used as a sort of map for locating the appropriate initial conditions for a true mixed state halo. For example, consider a halo where every particle is either in state 1 or state 2. If no particles are in state 2, table 4.1 gives an initial density of ${\mathcal{R}_0}^2 = .4130$. If all but one of the particles is in state 2, then ${\mathcal{R}_0}^2 = .02497$ for the lone state 1 particle. Based on these two extremes, it is possible to estimate the value of ${\mathcal{R}_0}^2$ for a state 1 particle in a halo with an any ratio states 1 and 2. ${\mathcal{R}_0}^2$ for state 2 can likewise be estimated.

Using these ranges, a solution can be acquired for a halo half in the ground state and half in the first excited state. The values of ${\mathcal{R}_0}^2$ are found to be .2204

and .1134 for states 1 and 2, respectively. The resulting halo density function has a core density value of .3338 and a median of 4.072. Figure 4.4 contains the plotted solutions. On the left panel are the individual wave functions for each state, and on the right is combined halo density function. It is similar in form to the ground state solution, except for a noticeable tail formation brought about by the contribution of the $n = 2$ state.

It can be seen from Table 4.1 that the quantity ${\mathcal{R}_0}^2 \times {\xi_{1/2}}^3$ is nearly constant for each n value regardless of N. The reason for this is simple. Any solution must be normalized to an area of 1 to reflect the fact that the particle has 100% chance of being found *somewhere* in space. Take the simple example of a two dimensional rectangle with length l, height h, and constant area 1. In order to preserve both the area and the shape, if l is increased then h must be decreased by some predictable amount. In this case $l \times h = 1$, so the height will always be $h = 1/l$.

A similar situation arises in the wave functions of quantum mechanics. For example, the potential in a hydrogenic atom is proportional to $-Z/r$, where Z is the atomic number. When Z is increased, the wave function gains a larger central density and a smaller Bohr radius, but its functional form (and thus its shape) remain constant (Merzbacher 1997). The potentials (Figure 4.2) that produce the wave functions in Figure 4.3 have nearly identical shapes, differentiated only by the number of small bumps they contain. The resulting wave functions are similar enough in appearance that when normalized, the product of their *height* (${\mathcal{R}_0}^2$) and *length* (represented in three dimensions by ${\xi_{1/2}}^3$) will be about the same. This relation can be useful in extrapolating Table 4.1 to values of $N > 3$.

Even with estimations of some initial conditions, solutions to a nonlinear two body problem such as this one are difficult to acquire. Still, these results show that such solutions are permitted by the equations, and their properties offer a glimpse

into the sorts of scales and shapes made possible even without the addition of external potentials. As the percentage and depth of excited states is increased, it's clear that the effective radius of the halo will increase and that the tail-like formation can be extended.

4.3 Effects of Nonlinearity on the Eigenstates

The potential of a given halo is a cumulative result of the mutual interaction all the individual particles. Under the Hartree approximation used in this analysis, if even one particle changes state, the entire potential changes (if only by an infinitesimally small amount). If the potential changes, so do the energy values of all the states of the halo. This makes it difficult to compare energy eigenstates, or even determine what is the ground state in all cases. In a linear system when a particle jumps to a more excited state, its energy should goes up by a predictable amount. But in doing so, the particle takes on a less dense wave function, spreading out its density over a larger volume. In the nonlinear case, this spreading has the effect of lowering the magnitude of the potential created by that particle's density function. This in turn lowers the energy eigenvalues of *all* the states in the halo.

This has several implications. First, it's not immediately clear whether one set of states represents a higher energy state than another. The ground state of the Helium atom is the one in which both electrons occupy the lowest energy orbital. If the $n = 1$ shell and the $n = 2$ shell each contain one electron, this certainly represents a more energetic atom. If instead the potential depended strongly on the wave functions of the individual electrons, it would not be as easy to determine which of these configurations has lower energy. It's possible that the ground state for this hypothetical *nonlinear* Helium atom could be the one in which one of the electrons occupies $n = 2$. For the S/P system, this opens up the possibility that the ground

state for a DM halo may not always be the one in which all the particles fall into the apparent $n = 1$ state. This means that variations between halos, such as total halo mass and luminous matter distributions, could affect the configuration of the ground state. This in turn would result in significant variations in halo shape.

Furthermore, since every possible combination of states for a halo represents a unique potential, there are no excited states for the halo itself. For each halo potential a (possibly infinite) number of individual eigenstates can be derived (ground state, first excited state, and so on), even if not all of those states are represented within the halo. If any of the particles changes state, every particle will be under the influence of a new potential. Thus there is no degeneracy among the energy levels of the particles, and each halo is its own ground state.

The possibility of BECs with nodes was explored by Kalas et al. (2010), whose model consisted of a BEC in an attractive finite well potential. As the depth of the well was increased, they noted that stable noded solutions occurred at discrete intervals of well depth, with all other depth values providing no stable noded solutions. This demonstrates that the inclusion of an external potential can actually induce nodes in a BEC wave function, and that two otherwise identical potentials with different magnitudes can result in dramatically different bound state behavior.

4.4 Summary

Stable excited single-state and multi-state solutions to the Schrödinger-Poisson only system were computed and their properties compared to known halo types. Placing every particle in the halo into the same excited state resulted in a wave function with a larger median and smaller core density, as well as a wave-like galactic rotation curve resembling that of many observed galaxies. Placing single particles of one state into a halos of particles with another state, a map was created which

constrained the likely initial conditions for an arbitrary halo composed of two different states. This map was used to narrow down the initial conditions of a halo half in ground and half in the first excited state. The density of this halo resembled the S/P only density but with a noticeable tail formation.

Admitting excited states expanded the gravitational S/P model to incorporate a larger range of DM halo types even without considering the addition of external potentials. Table 4.1 and the results from Figure 4.4 show the range of core density and median values that can occur as a result, even when the particle mass is held constant. In particular, Figure 4.4 shows the beginnings of a tail formation as a result of half the halo being in the first excited state.

CHAPTER 5

THEORETICAL FRAMEWORK

The results obtained in the previous chapters provide a window into the range of possible forms a quantum dark matter halo might take. It is worthwhile to examine the theoretical construct considered up to this point, including the assumptions made and the limitations incurred. This chapter will make a thorough examination of the S/P system and its limitations, and offer a purely analytical power series solution. In addition, the Einasto density profile so motivated by recent observations of DM halos will be examined for its viability as a solution to the Schrödinger equation.

5.1 The Schrödinger-Poisson System

5.1.1 Boundary Conditions

Since the problem involves simultaneously solving two differential equations, there are two sets of boundary conditions to consider. Solutions to the Schrödinger equation must be continuous, and so must $R'(r)$ wherever the potential is finite. In addition, $R(r)$ must be normalizable, which adds the constraint that $R(r \to \infty) = 0$. Common practice is to rewrite the equation in terms of a radial wave function $u(r) = rR(r)$, so that

$$u''(r) = \frac{2m}{\hbar^2}(V(r) - E)u(r). \tag{5.1}$$

Eq. (5.1) is a valid description for the wave function at all points except for $r = 0$, where $R(r \to 0) = [u(r)/r]_{r\to 0} \to \infty$. This problem can be handled in most cases by requiring that $u(r)$ vanish at the origin, so that $u(0) = [rR(r)]_{r\to 0} = 0$ (Merzbacher 1997). In this case, the behavior of R at the origin is constrained to

$R \approx r^k$, where $k > -1$. Even with this requirement Eq. (5.1) still permits some singular wave functions where $-1 < k < 0$, but these solutions are normalizable at the origin. For any lower power of r at $R(0)$, the total probability will be infinite.

This leaves open the question of $u(0) \neq 0$. Clearly $u(0) \not\to \pm\infty$, since such a solution would not be normalizable. $u(0) = const$ is normalizable, however. In this case $R(r) \approx 1/r$ at the origin.

If the considered wave function is finite-valued at the origin, then the potential must satisfy boundary conditions in the Poisson equation such that $V(0) = const$ and $V'(0) = 0$. This results in a flat, cored potential at the origin. It is easy to see from this requirement why the S/P only system will always produce a smooth-cored density profile. In the neighborhood of a local minimum a potential can be approximated as parabolic, and the wave function in that region can be approximated by a Gaussian function (Griffiths 2004). It is natural then for the S/P only wave function to have zero slope at the origin.

When adding external potentials to the picture, some of these boundary conditions become relaxed. Adding a black hole to the Schrödinger equation, for example, gives the potential a singularity at the origin. That singularity permits the wave function to have a cusp, while the potential produced by the Poisson equation retains its smooth core, satisfying the boundary conditions.

5.1.2 Symmetry and Degeneracy

The model considered in this dissertation assumed a spherically symmetric wave function. This decision is well-motived by observations (Burkett 1995; Ackermann et al. 2011; Chemin et al. 2011; Salvador-Solé et al. 2011), which indicate approximately spherical distributions in galactic halos. In reality there will always be fine deviations due to things like luminous matter distributions and hot gases. These deviations

should be largest for galaxies with the smallest mass-to-light ratios and in galaxies where the dark and luminous distributions are most coincidental. Simulations of galactic DM tend to produce slightly triaxial halos for spiral galaxies due to the spherical asymmetry of their luminous portions, with the galactic axis being stunted compared to the others (Jeon et al. 2009). Simulated elliptical galaxies also tend to have triaxial halos, with the axis lengths being of similar proportion to their luminous distributions (Knebe and Weibner 2006; Sales et al. 2012). In every case, the simulated halos do not deviate much from spherical symmetry.

Deviations may also occur as a result of angular momentum. For any spherically symmetric potential, including the hydrogen atom, the Schrödinger equation can easily be separated into angular and radial equations and solutions for each equation can be derived independently of the other. Indeed, the solutions to the angular equation are the same regardless of the potential; they are the well-known spherical harmonics. When $l = 0$, the angular solution is just the constant $1/\sqrt{4\pi}$, and so the entire wave function depends only on the radial component R(r). The solutions lose their spherical symmetry for $l > 0$, but as long as the potential remains symmetric, the equations can be treated separately.

In a nonlinear system, the picture is not as clear-cut. For the S/P system, if the wave function is not symmetric, neither is the potential. If even a small percentage of the particles in the halo have angular momentum $l > 0$, the potential derived through the Poisson equation gains a non-radial component. In this case, the Schrödinger equation is no longer separable into radial and angular components, turning the problem into a three dimensional nonlinear system of equations. Approximate symmetry is recovered for the halo, however, if the angular position is assumed to have a random phase factor.

5.1.3 Compton Wavelength and the Uncertainty Principle

As mentioned in the introduction, the incredibly small mass associated with a QDM particle implies a Compton wavelength $\lambda_c = \hbar/mc$ relevant on a galactic scale. A particle with a mass of 10^{-24} eV, for example, has a Compton wavelength on the order of 10 pc (Sin 1994). If the solar system has a DM density of $\sim 10^{-22}$ kg/m^3, this would put the classical interparticle distance at around 10^{-15} m (Sin 1994). In addition, there would be on the order of 10^{89} particles occupying a sphere with radius $\frac{1}{2}\lambda_c$. Thus both the quantum wave functions and the Compton wavelengths are heavily overlapping.

A consequence of the uncertainty principle is that the uncertainty in position must be at least one-half the Compton wavelength. This can be quantified by

$$\sigma_r \geq \frac{1}{2}\lambda_c \ , \tag{5.2}$$

where σ_r is the standard deviation. This provides an interesting dilemma. For the S/P system, as the mass of the halo increases, its radius gets smaller. As the halo becomes more and more compact, σ_r becomes smaller. At some point either Eq. (5.2) must be violated, or the halo will no longer obey the Schrödinger equation. On the other hand, it's possible either a new term in the potential or a new exclusion principle could be brought to bear on this problem.

5.1.4 The Hartree Approximation

Due to the large scale of the wave function involved, it may be that the Poisson equation does not produce a reasonable estimate of the potential. Use of the Hartree approximation assumes that each individual wave interacts with its neighbors as if they were point particles. Given that the waves are spread out on a scale of kiloparsecs, the time it takes for a force mediator to cross from one end of the halo

to the other is on the order of billions of years. In this case, it may be that local interactions outweigh contributions from the entire extended halo.

5.1.5 Power Series Solution

Though an Einasto profile with $n = 0.56$ offers a good approximation of the solution to the S/P only system, an exact solution can be found in the form of a power series. The equations of the Schrödinger-Poisson system can be written as a single differential-integral equation in the form

$$u''(r) = \left[\mathcal{B}\int_{\infty}^{r} \frac{1}{r'^2}\left(\int_{0}^{r'} u(r'')^2\, dr''\right) dr' - \mathcal{D}\right] u(r). \tag{5.3}$$

The solution, written in terms of $u(r) = rR(r)$, should satisfy the boundary conditions

$$u(0) = 0\ ,\ and \tag{5.4}$$

$$u(r \to \infty) = 0\ , \tag{5.5}$$

as well as the normalization condition

$$\int_{0}^{\infty} u(r)^2\, dr = 1\ . \tag{5.6}$$

Writing the radial function $R(r)$ as a power series,

$$R(r) = a_0 + a_1 r + a_2 r^2 + a_3 r^3 + \cdots = \sum_{n=0}^{\infty} a_n r^n\ , \tag{5.7}$$

$u(r)$ becomes

$$u(r) = rR(r) = a_0 r + a_1 r^2 + a_2 r^3 + a_3 r^4 + \cdots = \sum_{n=0}^{\infty} a_n r^{n+1}\ , \tag{5.8}$$

with the derivatives

$$u'(r) = a_0 + 2a_1 r + 3a_2 r^2 + 4a_3 r^5 + \cdots = \sum_{n=0}^{\infty} (n+1) a_n r^n \quad and \tag{5.9}$$

$$u''(r) = 2a_1 + 6a_2 r + 12a_3 r^2 + \cdots = \sum_{n=0}^{\infty}(n+1)(n+2)a_{n+1}r^n \ . \tag{5.10}$$

Anticipating the need in Eq. (5.3), $u(r)^2$ can be written as

$$u(r)^2 = \sum_{n=0}^{\infty} a_n r^{n+1} \times \sum_{m=0}^{\infty} a_m r^{m+1}$$

$$= {a_0}^2 r^2 + 2a_0 a_1 r^3 + (2a_0 a_1 + {a_1}^2)r^4 + (2a_0 a_3 + 2a_1 a_2)r^5 + \cdots$$

$$= \sum_{n=0}^{\infty} r^{n+2} \left[\sum_{m=0}^{\infty} a_m a_{n-m}\right] \ . \tag{5.11}$$

Plugging Eqs. (5.8), (5.10), and (5.11) into Eq. (5.3), the coefficients are found to be

$$a_n = \frac{1}{n(n+1)}\left(a_{n-2}\mathcal{D} + \mathcal{B}\sum_{m=0}^{n}\left[\frac{a_{n-m}}{(m+2)(m+3)}\sum_{q=0}^{m} a_q a_{m-q}\right]\right) \tag{5.12}$$

for even integer $n \geq 2$. The final solution for $R(r)$ is then

$$R(r) = \sum_{n=0}^{\infty} r^{2n}\frac{(2n-1)!}{(2n+1)!}\left(a_{n-2}\mathcal{D} + \mathcal{B}\sum_{m=0}^{n}\left[\frac{a_{n-m}}{(m+2)(m+3)}\sum_{q=0}^{m} a_q a_{m-q}\right]\right) \tag{5.13}$$

where $a_{n<0} = 0$.

Figure 5.1 shows the series progression as more and more terms are added, up to a maximum of 50 terms.

5.2 The Einasto Profile

The NFW density profile is one of the oldest dark matter fitting profiles still in use (Navarro et al. 1996; Navarro et al. 2010). As mentioned in Chapter 2, its density approaches infinity as $r \to 0$ and its mass function diverges as $r \to \infty$. Still, it has been very successful in fitting simulated DM halos to a finite inner radius and an applied cutoff virial radius. In real halos, it performs best in fits of large-scale galactic halos. Its steep inner slope, however, makes it a poor fit for so-called 'cored'

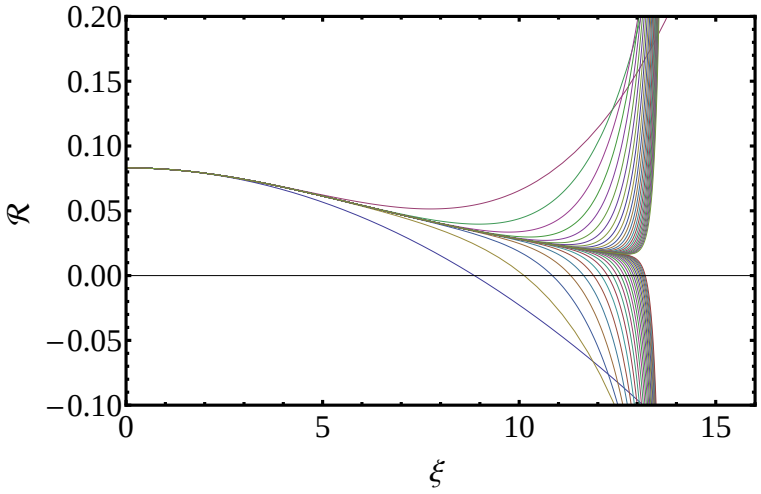

Figure 5.1. Graph showing the approximation of power series expansion of the S/P solution as more and more terms are added (50 total). The leftmost blue line contains only the first term; the leftmost red line the first two terms; etc., out to a total of 50 terms.

halos, whose densities flatten out toward the origin (Power et al. 2002; Navarro et al. 2004). The halos of these galaxies are better fit by the modified isothermal profile (ISO), as shown in (de Blok and Bosma 2002; Kuzio de Naray et al. 2006; de Blok 2010). As with the NFW profile, a cutoff radius must be applied to the ISO profile in order to avoid a divergent mass at $r \to \infty$.

The NFW and ISO density profiles have the form of broken power laws, with parameters representing the scales in which the density ρ and the radius r are measured. Such two-parameter models can effectively account for differences in magnitude and range, but they possess only one unique shape (cuspy profiles for NFW; smooth-cored profiles for ISO). The Einasto profile is a three-parameter model, having both the two scaling parameters and an additional shape parameter, n. The third parameter can produce either a cuspy ($n \geq 1$) or smooth-cored ($n < 1$) density distribution. This allows the Einasto profile to describe a much larger variety of halos, but at the expense of being a more general formula. Recent results have singled out the Einasto

profile as the overall best fit for modeling DM halos (Navarro et al. 2010; Chemin et al. 2011).

Astronomers have long sought after a universal density profile for dark matter halos (Merritt et al. 2005; Navarro et al. 2010). Even if a three-parameter model like the Einasto profile is successful in describing most dark matter halos, it won't be considered a universal profile unless physical constraints can reduce the number of parameters to two (Navarro 2010).

In fitting DM halos to both NFW and ISO profiles, several authors (e.g. Spano et al. 2008; Donato et al. 2009; Kormendy et al. 2009) have demonstrated a correlation between the model parameters, namely $p_c \propto 1/r_c$, where p_c and r_c are the characteristic density and radius of those models. This result suggests the presence of a hidden constraint on the DM structure formation.

Chemin et al. (2011) took velocity curve data from The HI Nearby Galaxy Survey survey (THINGS) and fit a number of galaxies to Einasto profiles. They note that in these fits the characteristic density and radius also have an apparent correlation, $p_{-2} \propto 1/r_{-2}^{1.6\pm0.1}$, though not all the halos modeled in the survey are well-constrained by this relation. If such a relation could indeed be established though observational evidence, it would bring the Einasto profile a step closer to being a universal description of DM distributions.

The functional form of the Einasto profile adopted by Navarro et al. (2010) and Chemin et al. (2011) is

$$\rho(r) = \rho_{-2}\ e^{-2n((r/r_{-2})^{1/n}-1)}\ , \tag{5.14}$$

where r_{-2} is the radius at which the logarithmic slope equals -2 and ρ_{-2} is the density at r_{-2}. This form is partly motivated by the fact that -2 is the slope of the modified isothermal profile as it approaches infinity. It also has the advantage that for most

Galaxy	ρ_{-2}	r_{-2}	n
NGC2366	5.7 ± 1.1	3.2 ± 0.3	1.1 ± 0.2
NGC5055	1.3 ± 0.1	22.6 ± 0.6	0.5 ± 0.1
NGC3621	0.3 ± 0.2	39.9 ± 12.3	6.4 ± 1.0
NGC2403	1.6 ± 0.3	15.3 ± 1.8	4.1 ± 0.4
NGC3198	2.2 ± 0.3	13.0 ± 0.7	2.0 ± 0.3

Table 5.1. Characteristic mass densities, radii, and Einasto indices for fits to the dark matter halos of five galaxies based on velocity curve data from the THINGS galaxy survey. Columns from left to right: Galaxy designation; characteristic density in 10^3 solar masses/kpc^3; characteristic radius in kpc; and Einasto index. Source: Chemin et al. (2011)

real galaxies the values of ρ_{-2} and r_{-2} fall within a magnitude (or at most two) of one another, regardless of the value of n.

A sampling of the fitting data from Chemin et al. (2011) is provided in Table 5.1. The authors also provided fits to NFW and ISO profiles for these same galaxies. They note that the Einasto profile provides the best overall fit.

5.2.1 Einasto in the Schrödinger-Poisson System

A natural solution to the S/P system is one in which the potential produced by a density in the Possion equation is the same potential that gives rise to that density in the Schrödinger equation. A generalized Einasto wave function can be constructed taking a simple form,

$$R(r) \sim e^{-(r/r_0)^{1/n}} \ , \tag{5.15}$$

and normalizing it to get

$$|R(r)| = \frac{e^{-\left(\frac{r}{r_0}\right)^{\frac{1}{n}}}}{\sqrt{8^{-n} n r_0^3 \Gamma(3n)}} \ , \tag{5.16}$$

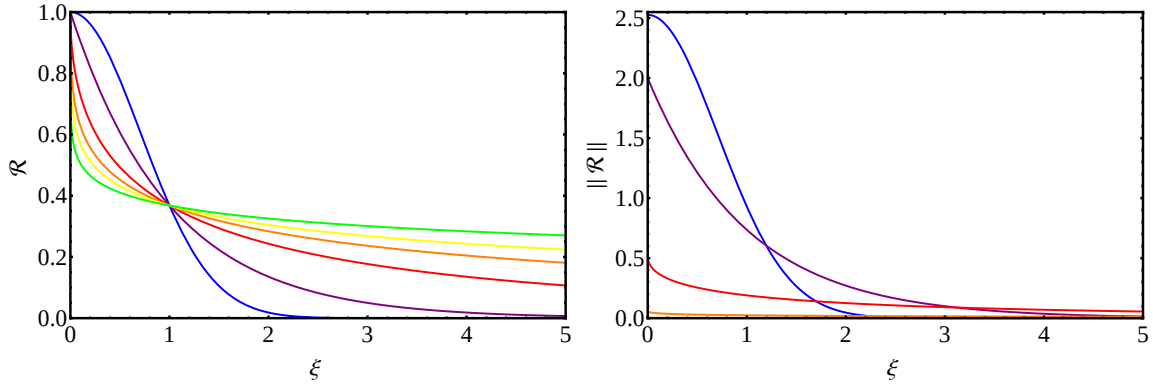

Figure 5.2. Comparison of the unnormalized (left panel) and normalized (right panel) Einasto wave functions for $r_0 = 1$ and $n = 1/2$ [blue]; 1 [purple]; 2 [red]; 3 [orange]; 4 [yellow]; and 6 [green].

where Γ is the gamma function. Then letting $R_0 = 1/\sqrt{8^{-n} n r_0^3 \Gamma(3n)}$, the normalized probability density becomes

$$|R(r)|^2 = {R_0}^2 \; e^{-2(r/r_0)^{1/n}} \; . \tag{5.17}$$

The derivative is given by

$$R'(r) = -\frac{R_0}{n r_0} \left(\frac{r}{r_0}\right)^{\frac{1}{n}-1} e^{-\left(\frac{r}{r_0}\right)^{\frac{1}{n}}} \; , \; n \neq 1, \tag{5.18}$$

or $R'(r) = -\frac{R_0}{r_0} e^{-\left(\frac{r}{r_0}\right)^{\frac{1}{n}}}$ for $n = 1$. Einasto profiles can be divided into two categories based on the value of this derivative at zero. Cuspy Einasto profiles have a central derivative of either $-R_0/r_0$ ($n = 1$) or $-\infty$ ($n \geq 1$), while smooth profiles ($n < 1$) have a value of 0.

Figure 5.2 shows the unnormalized (left panel) and normalized (right panel) Einasto wave functions. When normalized, Einasto profiles with larger n values take on very, very small central probability densities (and very large effective radii). This correlates well with the fact that higher mass halos tend to be fit better with larger n. Since more massive halos are also spread out over a larger area, if those halos are represented by a wave function, that wave function will have a lower overall density.

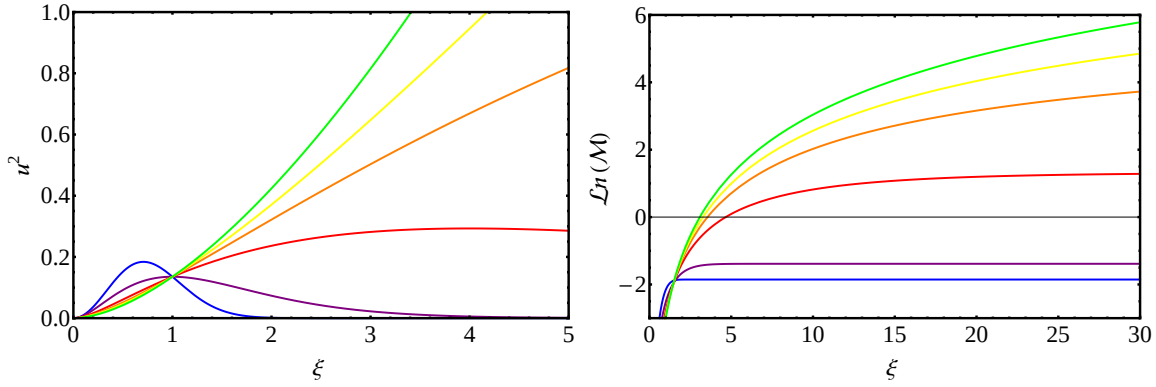

Figure 5.3. Comparison of the unnormalized linear probability density u^2 (left panel) and the resulting logarithmic mass functions (right panel) for $r_0 = 1$ and $n = 1/2$ [blue]; 1 [purple]; 2 [red]; 3 [orange]; 4 [yellow]; and 6 [green].

Figure 5.3 shows the unnormalized linear probability density u^2 (left panel) and the resulting logarithmic mass functions (right panel), which give an idea how quickly the mass converges as a function of radius. Figure 5.4 shows the velocity curves for the unnormalized (left panel) and normalized (right panel) Einasto wave functions. As r approaches the virial radius, the mass function approaches a constant value and the velocity curve approaches $1/r^{1/2}$. The right panel of Figure 5.4 shows how quickly these curves approach $1/r^{1/2}$ for the normalized Einasto functions. From all these figures it can be seen that the lower values of n virialize more quickly.

For an unspecified n, the potential given by the Poisson equation for an Einasto density $p(r) = MR_0{}^2\ e^{-(r/a)^{(1/n)}}$ is given by

$$V_{Pois} = GmMR_0{}^2nr_0{}^3\left[\frac{\Gamma\left(3n, 2(\frac{r}{r_0})^{\frac{1}{n}}\right)}{8^n r} - \frac{\Gamma(3n)}{8^n r} - \frac{1}{r_0 4^n}\Gamma\left(2n, 2\left(\frac{r}{r_0}\right)^{\frac{1}{n}}\right)\right], \quad (5.19)$$

where the single-argument Γ is the Euler Gamma function and the double-argument Γ is the incomplete gamma function defined by $\Gamma(a, y) = \int_y^\infty x^{a-1}e^{-x}dx$.

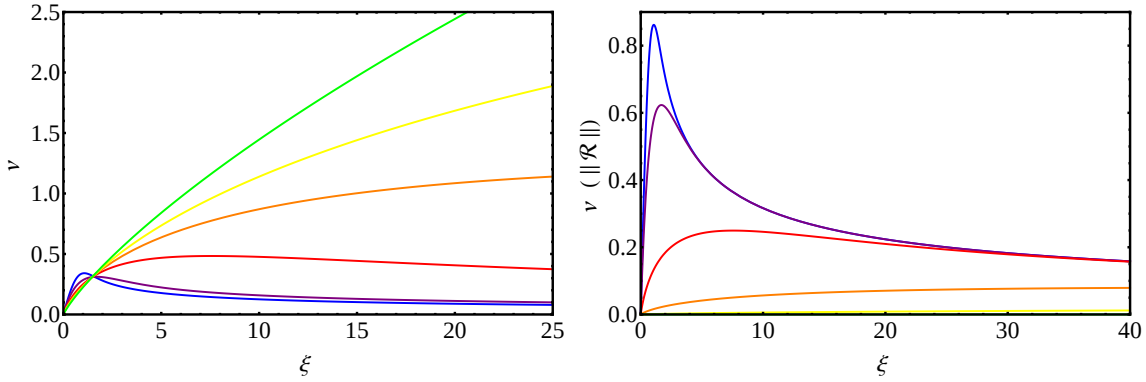

Figure 5.4. Comparison of the radial velocity curves for the unnormalized (left panel) and normalized (right panel) Einasto wave functions for $r_0 = 1$ and $n = 1/2$ [blue]; 1 [purple]; 2 [red]; 3 [orange]; 4 [yellow]; and 6 [green].

By rearranging the Schrödinger equation, it is possible to find the potential which would produce that same Einasto density as a ground state solution:

$$V_{Schro} = \frac{\hbar^2}{2m}\frac{\nabla^2 R}{R} + E \ . \tag{5.20}$$

For the Einasto profile this becomes

$$V_{Schro} = \frac{\left(\frac{r}{a}\right)^{2/n}}{n^2 r^2} - \frac{\left(\frac{r}{a}\right)^{\frac{1}{n}}}{n^2 r^2} - \frac{\left(\frac{r}{a}\right)^{\frac{1}{n}}}{nr^2} \ . \tag{5.21}$$

Figure 5.5 gives the potentials produced by the Poisson equation (left panel) and the Schrödinger equation (right panel) for various n values. The Einasto profile is not an exact solution to the S/P system, and the potentials produced from each equation are quite different in form. However, as discussed in previous chapters, the true galactic potential will always be a combination of the halo potential and the contributions of baryonic matter distributions, among other things.

From Figure 5.5 it's clear that Einasto profiles with $n \geq 1$ are produced by singular potentials. In particular, an Einasto profile with $n = 1$ is the solution to the Schrödinger equation with potential $\propto -1/r$. An $n = 2$ profile is the solution when

$$V_{Schro} = \frac{1}{4r} - \frac{3}{4r^{3/2}} \ , \tag{5.22}$$

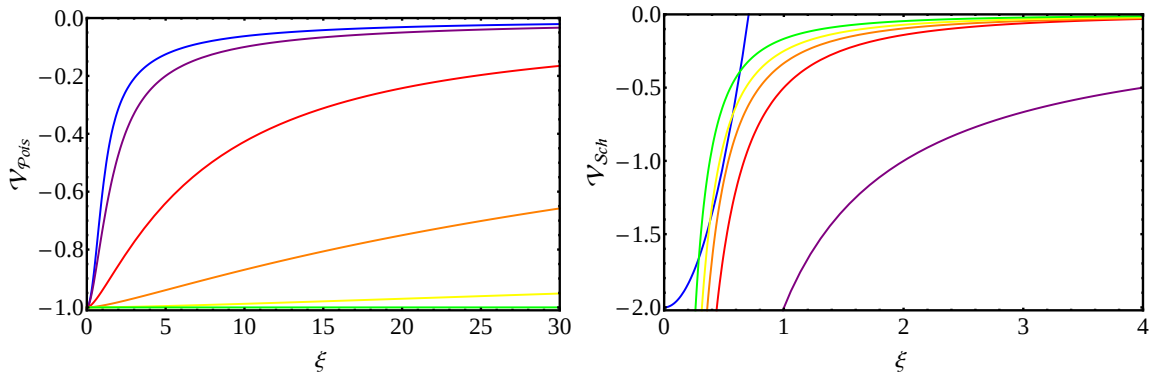

Figure 5.5. Comparison of the potentials produced by the Poisson equation (left panel) and the Schrödinger equation (right panel) for the Einasto wave functions with $r_0 = 1$ and $n = 1/2$ [blue]; 1 [purple]; 2 [red]; 3 [orange]; 4 [yellow]; and 6 [green].

which is even more singular than the one produced by a black hole. For $n = 3$,

$$V_{Schro} = \frac{1}{9r^{4/3}} - \frac{4}{9r^{5/3}} \ , \tag{5.23}$$

which is more singular still. In fact, as $n \to \infty$ the potential in the Schrödinger equation approaches $\propto -1/r^2$. It is interesting to point out that this is the potential produced by a point source in four dimensions, and the Einasto profiles could be thought of as the natural solutions to the Schrödinger equation with a point source potential in an arbitrary finite positive rational number of dimensions. However, fractal dimensions are outside the scope of this dissertation.

5.2.2 The Generalized Normal Distribution

The Einasto profile in astrophysics is equivalent in form to the generalized normal distribution (GND) in statistics (Varanasi and Aazhang 1989; Nadarajah 2005). The special case of $n = 0.5$ is the well-known Gaussian distribution describing how a large number of identical random variables given equal weight will distribute themselves about the mean. In quantum mechanics, the Gaussian is the ground state

solution to the one-dimensional harmonic oscillator. The associated potential, $\sim r^2$, is the same as that created inside a region of constant charge density in three dimensions. The Einasto profile with $n = .56$ is very close to Gaussian, and the potential created by its relatively flat (constant density) core very closely approximates r^2 in this inner region, which helps explain its shape. As n is increased and the flatness of the core diminishes, the potential it creates no longer reproduces the original density. This means that a self-interacting Poisson potential alone is not enough to produce Einasto profiles with general n.

The n parameter is correlated with the statistical property of kurtosis, the fourth moment of a distribution. A higher n value produces a higher kurtosis, and a higher kurtosis means a sharper central peak and a thicker tail. Statistically, in a Gaussian, constituents are given equal weight across the entire range. GND with a higher kurtosis give more weight to individuals farther from the expected value. Empirically, GND with higher n values often occur as a result of additional sources of error, such as in resolving acoustical data from high background noise (Varanasi and Aazhang 1989). Though GND are commonly used in statistical analysis, the precise causes of this extra error are not always well-understood.

Several authors (Navarro 2010; Merritt et al. 2006; Gao et al. 2008) have pointed out that the mass of the halo may be correlated with n, with higher mass halos having higher n values. It's possible that the higher degree of kurtosis observed in large galaxies may be a direct result of the Heisenberg Uncertainty Principle. Given the enormous particle population, the uncertainty in position may be compounded in some nonlinear way. The addition of various distributions of baryonic matter could also have unpredicted effects on the uncertainty.

5.3 Summary

In this chapter, the assumptions and limitations of the gravitational Schrödinger-Poisson system were discussed; a power series solution to the problem was presented; and the Einasto profile was examined as a solution to the Schrödinger equation.

The gravitational Schrödinger-Poisson system with an extremely light bosonic particle is a complex nonlinear problem which in many ways tests the boundaries of its constituent equations. Like many nonlinear problems, it is highly susceptible to the choice of initial conditions, and common first-order assumptions like spherical symmetry can also have unexpected effects.

Although the S/P only solution is well-represented by an Einasto profile with a single index ($n \approx 0.56$), modifications to the system such as the inclusion of baryonic matter potentials are able to expand the range of n. In addition, the Einasto family includes two well-known solutions to the Schrödinger equation, the hydrogenic atom and the quantum harmonic oscillator, the latter solution doubling as the Gaussian distribution in statistics. These facts together with Einasto's success in describing real galactic DM halos motivate its use as a fitting model for QDM halos.

CHAPTER 6

CONCLUSIONS AND FUTURE WORK

The QCDM models originally introduced by Sin (1994) and later modified by Hu et al. (2000) were successful at addressing the long-standing flaws in CDM simulations, the highly cusped profiles they produced and the overabundance of low-mass halos they predicted. In this dissertation, a comprehensive gravitational Schrödinger-Poisson system was developed to test the predictions of these models against the most recent observational evidence. A power series solution to this system was provided in Chapter 5. Numerical results were presented in Chapter 2, and the following conclusions were drawn:

- The solutions to the QCDM models are well-approximated by an Einasto profile with an index of $n \approx 0.56$. This smooth-cored profile is a good description for many smaller dwarf galaxies, which are best-fit by Einasto profiles with $n < 1$ (Chemin et al. 2011).
- The models cannot account for the variety of observed halo shapes. Like the NFW and modified isothermal profiles, the ground state QCDM density has the same shape regardless of the mass or size of the halo. Since real high-mass galaxies can be fit to Einasto distributions with higher n values, the overall scope of these models is limited.
- The QCDM models also cannot account for the size and total mass of observed halos without invoking a different particle mass for each halo.

To expand the applicability of such QCDM models, stable ground state solutions to the Schrödinger-Poisson system with additional potentials were computed and

their properties compared to known halo types. In particular, the effects of the galaxy's baryonic matter content were considered, as well as the inclusion of a particle scattering term. With the addition of a supermassive black hole at the galactic center:

- The halo adopted a more peaked distribution associated with simulated DM halos and with observed halos in large galaxies.
- The DM content of the halo was drawn inward, producing a larger core density and smaller median radius.
- The galactic rotation curve achieved a higher maximum at a closer radius than the same galaxy with no black hole.
- The galactic potential gained a singularity that began to dominate the halo at small radii.
- As the black hole mass was increased, the Einasto index began to approach 1, expanding the overall range to $0.56 > n > 1$.

With the addition of a luminous matter distribution:

- The smooth-cored profile of the S/P only solution was preserved.
- LM distributions with small radii produced a more concentrated halo, with a larger core density and smaller median radius.
- LM distributions with large radii had a diffusing effect on the halo, giving it a smaller core density and larger median radius.
- The galactic rotation curve achieved its sharpest peak when the LM had the smallest radius and a mass comparable to the DM.
- The galactic potentials gained a visible well, with smaller values of LM median producing deeper wells closer to the origin, suppressing the appearance of a cusp.

With the addition of a Gross-Pitaevskii scattering term:

- The halo acquired a more rounded density profile, with the strongest terms resulting in an almost parabolic appearance.
- The halos were spread out over a larger volume, with smaller core densities.
- The addition of a black hole created some unusual halo shapes, and for certain values began to emulate the properties of Einasto profiles with $n > 1$.

Each added potential presented in this dissertation expanded the gravitational S/P model to incorporate a larger range of DM halo types, creating both cuspy and smooth-cored profiles as well as extending the possible range of central density and median radius values permitted.

In addition, stable excited single-state and multi-state solutions to the Schrödinger-Poisson system were computed, with the following results:

- Placing every particle in the same excited state resulted in a halo with a larger median and a smaller core density.
- These single-state halos produced wave-like galactic rotation curve resembling that of many observed galaxies.
- A method was developed to constrain the likely initial conditions for an arbitrary halo composed of two different states.
- This method was used to narrow down the initial conditions of a halo half in ground and half in the first excited state. The density of this halo resembled the S/P only density but with a noticeable tail formation.

Admitting excited states expanded the gravitational S/P model to incorporate a larger range of DM halo types even without considering the addition of external potentials.

QCDM may well be a viable theory, but it's far from complete. Despite all the expansions to the model presented here, none of the results produced approximates an Einasto profile with the highest n values observed in real galaxies. Further studies might be able to bridge that gap, however. There are several possibilities worth

exploring. As discussed in Chapter 3, a high-precision numerical analysis of the S/P system with both a black hole and a scattering term could yield a solution resembling an Einasto profile with an even higher n value. Also, an expanded study of excited and mixed states might prove worthwhile.

In addition, some less orthodox adjustments could be considered. For example, postulating a different interaction potential between the DM particles can change the entire picture. Many particles have potentials that change significantly depending on their proximity, for example. Surprisingly, the Hartree approximation can still be used in this approach, though in many cases the resulting halo potential is not analytic.

Since DM particles do not interact electromagnetically, they cannot radiate a photon to lower their energy level. A tantalizing notion is that they might radiate a graviton, or perhaps a gravitational wave, but this is unknown. If in fact they have no effective means of radiating, it is worth exploring a fractal explanation for their behavior of seeking out equilibrium configurations in the form of exponentials with fractional powers of r. These ideas are left as possible areas of future study.

APPENDIX A

COMPUTER CODE

```
//Gravitational Schrodinger-Poisson System
//RK4 Method

#include <math.h>
#include <stdio.h>
#include <dirent.h>
#include <dir.h>

//Constants
#define N 2                          //number of equations
//Coefficient of Potential Term
#define B 1.0
//Point Charge (SMBH) Potential
#define A1 0.0                       //Relative Strength of SMBH Potential
//LM Potential Einasto n = 1
#define G 0.99
#define A2 (1-G)/G                   //Relative Strength of LM Potential
#define a2re 32.0                    //LM median
#define d1 2.674566667               //d(n=1)
//LM Potential Einasto n = 4
#define A3 0.0
//Gross-Pitaevskii Term
#define C 0.0
//Hartree
#define n 1.0
#define A 0.1

//Dependents
#define MIN 0.0                      //minimum x
#define MAX 40.0                     //maximum x

#define MAXmod 1.0
#define dist (MAX/30000.0)           //stepsize

#define initialminslope 0.0          //Min slope
#define initialmaxslope 1.0*2.0      //Max slope
```

```
#define initialminD 0.0              //Min D (related to energy)
#define initialmaxD 1000.0*2.0       //Max D

#define initialV (-B*10)
#define Dthreshold 0.000000000000001 //level of precision for energy calculation
#define areathreshold 0.01
#define manualD 1.0                  //Set constant D when using manual mode
#define manualslope 0.5              //Set initial slope when using manual
#define manualcutoff 100.0           //Cutoff x value for output files
#define automated 1                  //0 = manual, 1 = automated

//Definition of Equations - This is the SE with Poisson Potential
double  f(double x, double y[], int i, double D, double Vofx)
{
   if (i == 0)
   {
      return(y[1]);    // RHS of first equation
   }
   else
   {
      if (x == 0.0)
      {
         return(0.0);
      }
      else
      {
// RHS of second equation:
//         return(y[0]*(B*Vofx+D));  // SP
//         return(y[0]*(D+A*(y[0]*y[0]/x/x)*(1-2/x)));  // Hartree
//         return(y[0]*(D-A*sqrt(sqrt((y[0]/x)*(y[0]/x)))));  // Hartree
//         return(y[0]*(B*(Vofx+A*y[0]*y[0]/(x*x))+D));  // Hartree + SIP
//         return(y[0]*(0.5*B*((exp(-d1*x/a2re)*(d1*x/a2re+2.0)-2.0)/x)
//                                                 +D));  // EIN only
//         return(y[0]*(0.5*A2*((exp(-d1*x/a2re)*(d1*x/a2re+2.0)
//                               -2.0)/x)+B*Vofx+D));  // SIP + EIN n1
/*         return(y[0]*
         (B*
         (Vofx+A2*(exp(-d1*x/a2re)*(1.0+d1*x/a2re)-1.0)/x)
         +D
```

```
        ));  // SIP + EIN n1 Generic
*/
        return(y[0]*(2.0*B*(Vofx-A1/x)+D-1.0));  // SP + BH
//        return(y[0]*(B*(Vofx-A1/x)+C*y[0]*y[0]/(x*x)+D));  // SP + GP +BH
//        return(y[0]*(B*(-A1/x)+C*y[0]*y[0]/(x*x)+D));  // GP + BH
//        return(y[0]*(D/1000.0+B*(exp(-2.0*x/1000.0)
//                                    -1)/x));  // Yukawa Approximation
//        return(y[0]*(D/1.0+B*(-3.0*sqrt(x)/(x*x)+1.0/x)));  // SchrodPot n2
//        return(y[0]*(D/1.0+B*(-1.0/x)));  // SchrodPot n1
//        return(y[0]*(D/1000.0-B*(log(x+1.0)/x)));  // PoissPot NFW
//        return(y[0]*(D/1000.0+B*(3.0*x*x-6.0*x-1.0)/
//                           (4.0*x*x*(x+1.0)*(x+1.0))));  // SchrodPot NFW
//        return(y[0]*(B*((-A1/x)+(exp(-2.0*sqrt(x))*(15.0+30.0*sqrt(x)+27.0*x
//        +14.0*x*sqrt(x)+4.0*x*x)-15.0)/(960.0*x))+D)); //BH plus PoissPot n2
/*        return
        y[0]*
        (
           B*
           (
              (
                 exp(-2.0*sqrt(sqrt(x)))*
                 (
                    155925.0/x+311850.0*sqrt(sqrt(x))/x+311850.0*sqrt(x)/x
                    +207900.0/sqrt(sqrt(x))+103635.0+40950.0*sqrt(sqrt(x))
                    +13230.0*sqrt(x)+3540.0*x/sqrt(sqrt(x))+780.0*x
                    +136.0*x*sqrt(sqrt(x))+16.0*x*sqrt(x)
                 )
                 -155925.0/x
              )
              /638668800.0-A1/x
//              /(4.0*x)-A1/x
           )
           +D/1000000.0
        );   */
          // BH plus PoissPot n4
//        return(y[0]*(B*x*x+D-10.0));  // SchrodPot n1/2 (Gaussian)
//        return(y[0]*(B*((10.0*exp(-1000.0*x*x*x*x*x*x*x*x*x*x*x)-1)/x)+D-5));
                                              // BH Pot with BH 'barrier'
     }
```

```
   }
}

// Runge-Kutta subroutine
void runge4(double x, double y[], double Dr, double Vr)
{
   double h=dist/2.0,
          t1[N], t2[N], t3[N],
          k1[N], k2[N], k3[N],k4[N];
   int i;

   for (i=0; i<N; i++) t1[i] = y[i]+0.5*(k1[i]=dist*f(x, y, i, Dr, Vr));
   for (i=0; i<N; i++) t2[i] = y[i]+0.5*(k2[i]=dist*f(x+h, t1, i, Dr, Vr));
   for (i=0; i<N; i++) t3[i] = y[i]+    (k3[i]=dist*f(x+h, t2, i, Dr, Vr));
   for (i=0; i<N; i++) k4[i] =                 dist*f(x + dist, t3, i, Dr, Vr);

   for (i=0; i<N; i++) y[i] += (k1[i]+2.0*k2[i]+2.0*k3[i]+k4[i])/6.0;
}

void runeq(double x, double y[], double De, double& Ve, double& I2e)
{
   if (x > 0.0)
   {
      I2e += y[0] * y[0];
      Ve += I2e * dist * dist / (x * x);
   }
   runge4(x, y, De, Ve);
}

//Calculates the area of the aquired solution
void findarea(double x, double y[], double Da, double slopea,
              double& areaa, double& cutoffa, double& mediana, double& finalVa)
{

   double u = 0.0, I2 = 0.0, halfarea = 0.0, V = initialV;

   y[1] = 0.0 + slopea;
   y[0] = 0.0;
   x = MIN;
```

```
   areaa = 0.0;
   cutoffa = 0.0;

   do
   {
      runeq(x, y, Da, V, I2);
      x += dist;
      if ((y[0] > (u*x/(x-dist)) || y[0] < 0)&&(x > dist*20.0))
      {
         cutoffa = x - dist;
      }
      else
      {
         u = y[0];
         areaa = areaa + dist * u * u;
      }
   }
   while (y[0] >= 0.0 && cutoffa == 0.0 && x < MAX);
   if (areaa <= 0.0) {areaa = 0.001;}
   if (cutoffa == 0.0) {cutoffa = MAX;}
   finalVa = V;

//Calculate Median
   y[1] = 0.0 + slopea;
   y[0] = 0.0;
   x = MIN;
   V = initialV;
   I2 = 0.0;
   do
   {
      runeq(x, y, Da, V, I2);
      x += dist;
      halfarea = halfarea + (dist * y[0] * y[0]);
   }
   while (halfarea < (areaa/2.0));
   mediana = x;

}
```

```
//Shooting Method to Find the Energy (D)
void findD(double x, double y[], double& var2D2, double floor,
                                                    double ceiling, double slope)
{
   double percentdiff, I2, V;

   do
   {
      y[1] = 0.0 + slope;
      y[0] = 0.0;
      x = MIN;
      I2 = 0.0;
      V = initialV;
      var2D2 = (ceiling + floor)/2.0;
      percentdiff = (ceiling - floor)/var2D2;

      do
      {
         runeq(x, y, var2D2, V, I2);
         x += dist;
      }
      while (x < MAX && y[0] >= 0.0);

      if (y[0] < 0.0)
      {
         floor = var2D2;
      }
      else
      {
         if (y[0] > 0.0)
         {
            ceiling = var2D2;
         }
         else
         {
            percentdiff = 0.0;
         }
      }
   }
```

```
   while (percentdiff >= Dthreshold);
//   var2D2 = ceiling;
}

//Output Data to Files
void outputs(double x, double y[], double nrg, int incnumber, double slope,
                              double cutoffo, double trueinitVo, double trueDo)
{
   char buffer[20];
   double expvaluenumer = 0.0, expvaluedenom = 0.0, expvalue = 0.0, halfarea = 0.0;
   double I2 = 0.0, V = initialV, dummy = 0.0, mediano = 0.0, areao = 0.0;

   y[1] = 0.0 + slope;
   y[0] = 0.0;
   x = MIN;

   sprintf(buffer, "%i", incnumber);
   mkdir(buffer);
   chdir(buffer);

   FILE *output, *output2, *output3, *output4;
   output = fopen("uofr.txt","w");
   output2 = fopen("psi.txt","w");
   output3 = fopen("psi2.txt","w");
   output4 = fopen("V.txt","w");
   do
   {
      runeq(x, y, nrg, V, I2);
      x += dist;
      fprintf(output, "%.16f\t%.16f\n", x, y[0]);
      fprintf(output2, "%.16f\t%.16f\n", x, y[0]/x);
      fprintf(output3, "%.16f\t%.16f\n", x, y[0]*y[0]/(x*x));
      fprintf(output4, "%.16f\t%.16f\n", x, V);
      if (x <= cutoffo)
      {
         expvaluenumer = expvaluenumer + (dist * y[0] * y[0] * x);
         expvaluedenom = expvaluedenom + (dist * y[0] * y[0]);
      }
   }
```

```
   while (x < MAX);

   fclose(output);
   fclose(output2);
   fclose(output3);
   fclose(output4);
   expvalue = expvaluenumer / expvaluedenom;

   findarea(x, y, nrg, slope, areao, cutoffo, mediano, dummy);


      output = fopen("median.txt","w");
      fprintf(output, "%f\n", mediano);
      fclose(output);
      output = fopen("stats.txt","w");
      output2 = fopen("stats-accum.txt","a");
      output3 = fopen("show-stats.txt","w");
//      fprintf(output, "B-------\tD(est)--\tD(raw)--\tslope---\tarea----
//                                      \tmedian--\tcutoff---\tVi(est)--\n");
//      fprintf(output, "B-------\tA-G-----\tLmedian-\tD(raw)--\tslope---
//                        \tarea----\tmedian--\tcutoff---\tMax-----\n");   //LM
      fprintf(output, "A-------\tn(Ein)--\tD(raw)--\tslope---\tarea----\
                               tmedian--\tcutoff---\tMax-----\n");   //Hartree

//      fprintf(output, "%f\t%f\t%f\t%f\t%f\t%f\t%f\t%f\n", B, trueDo, nrg,
//                                 slope, areao, mediano, cutoffo, trueinitVo);
//      fprintf(output, "%f\t%f\t%f\t%f\t%f\t%f\t%f\t%f\t%f\n", B, A2, a2re,
//                               nrg, slope, areao, mediano, cutoffo, MAX); //LM
      fprintf(output, "%f\t%f\t%f\t%f\t%f\t%f\t%f\t%f\n", A, n, nrg, slope,
                                      areao, mediano, cutoffo, MAX); //Hartree
      fprintf(output2, "%f\t%f\t%f\t%f\t%f\t%f\t%f\t%f\n", B, trueDo, nrg,
                                  slope, areao, mediano, cutoffo, trueinitVo);
      fprintf(output3, "%s\n", desc1);
//      fprintf(output3, "%s\n", desc2);   //SIP+EIN
//      fprintf(output3, "B-------\tA-------\tD(est)--\tD(raw)--\
//                                       tslope---\tmedian--\n");   //SIP+SMBH
//      fprintf(output3, "B-------\tA-------\tLMmedian\tD(est)--
//                               \tD(raw)--\tslope---\tmedian--\n");   //SIP+EIN
      fprintf(output3, "B-------\tA-BH----\tD(est)--\tD(raw)--\tslope---
```

```
                                                \tmedian--\n");   //SIP+GP
//      fprintf(output3, "%f\t%f\t%f\t%f\t%f\t%f\n", B, A1, trueDo,
//                                          nrg, slope, mediano);   //SIP+SMBH
//      fprintf(output3, "%f\t%f\t%f\t%f\t%f\t%f\t%f\n", B, A2, a2re,
//                                   trueDo, nrg, slope, mediano);   //SIP+EIN
       fprintf(output3, "%f\t%f\t%f\t%f\t%f\t%f\n", B, A1, trueDo,
                                            nrg, slope, mediano);   //SIP+GP
       fclose(output);
       fclose(output2);
       fclose(output3);
       chdir("..");
}

int main()
{
   double x, y[N], Dincrement, minD, maxD, minslope, maxslope;
   double area = 0.0, median = 0.0, finalV = 0.0, trueinitV, trueD;
   double cutoff = manualcutoff, slope = manualslope, varD = manualD;
   int j, incnum = 0;

   chdir("SP");
   chdir("BH");
   FILE *tester;

// Automated Section
   if (automated == 1)
   {
      minslope = initialminslope;
      maxslope = initialmaxslope;

      tester = fopen("log.txt","a");
      fprintf(tester, "B-------\tD(est)------------\tD(raw)-------------\
           tslope-------------\tarea----\tcutoff---\tmedian--\tVi(est)----\n");
      printf("B-------\tD(est)------------\tD(raw)-------------\
                       tslope-------------\tarea----\tcutoff---\tmedian--\n");

      do
      {
         minD = initialminD;
```

```
        maxD = initialmaxD;
        slope = (minslope + maxslope)/2;
        findD(x, y, varD, minD, maxD, slope);
        findarea(x, y, varD, slope, area, cutoff, median, finalV);
        trueinitV = 1.25*(initialV-finalV);
        trueD = varD+(B*initialV);
        fprintf(tester, "%f\t%.16f\t%.16f\t%.16f\t%f\t%f\t%f\t%f\n", B,
                        trueD, varD, slope, area, cutoff, median, trueinitV);
        printf("%f\t%.16f\t%.16f\t%.16f\t%f\t%f\t%f\n", B,
                                    trueD, varD, slope, area, cutoff, median);
        if (area < 1.0)
        {
           minslope = slope;
        }
        else
        {
           maxslope = slope;
        }
     }
     while (area < (1.0 - areathreshold) || area > (1.0 + areathreshold));
     fclose(tester);
  }

// Output Data
  maxD = varD * (1.0 + Dthreshold);
  minD = varD * (1.0 - Dthreshold);
  Dincrement = (maxD - minD) / 2.0;
  for (varD = minD; varD <= maxD; varD = varD + Dincrement)
  {
     incnum = incnum + 1;
     if (incnum == 2){
        outputs(x, y, varD, incnum, slope, cutoff, trueinitV, trueD);
     }
  }

  chdir("..");
  chdir("..");
  printf("FIN\n");
```

```
return 1;
}
```

REFERENCES

M. Ackermann, M. Ajello, A. Albert, W. Atwood, et al. Constraining Dark Matter Models from a Combined Analysis of Milky Way Satellites with the Fermi Large Area Telescope. *Physical Review Letters*, **107**, 2011.
URL `http://link.aps.org/doi/10.1103/PhysRevLett.107.241302`

D. Acosta-Kane, R. Acciarri, O. Amaize, M. Antonello, et al. Discovery of underground argon with low level of radioactive 39Ar and possible applications to WIMP dark matter detectors. *Nuclear Instruments and Methods in Physics Research Section A: Accelerators, Spectrometers, Detectors and Associated Equipment*, **587**:46, 2008.

A. Aguirre, J. Schaye, and E. Quataert. Problems for Modified Newtonian Dynamics in Clusters and the Ly Forest? *The Astrophysical Journal*, **561**:550, 2001.
URL `http://iopscience.iop.org/323376`

Z. Ahmed, D. S. Akerib, S. Arrenberg, C. N. Bailey, et al. Results from a Low-Energy Analysis of the CDMS II Germanium Data. *Physical Review Letters*, **106**:131302, 2011.

I. F. M. Albuquerque and L. Baudis. Direct Detection Constraints on Superheavy dark matter. *Physical Review Letters*, **90**:221301, 2003.

M. H. Anderson, J. R. Ensher, M. R. Matthews, C. E. Wieman, et al. Observation of Bose-Einstein Condensation in a Dilute Atomic Vapor. *Science*, **269**:198, 1995.
URL `http://www.sciencemag.org/content/269/5221/198`

G. W. Angus, B. Famaey, and H. S. Zhao. Can MOND take a bullet? Analytical comparisons of three versions of MOND beyond spherical symmetry. *Monthly Notices of the Royal Astronomical Society*, **371**:138, 2006.

S. Archambault, F. Aubin, M. Auger, E. Behnke, et al. Dark matter spin-dependent limits for WIMP interactions on 19F by PICASSO. *Physics Letters B*, **682**:185, 2009.

S. J. Asztalos, E. Daw, H. Peng, L. J. Rosenberg, et al. Experimental Constraints on the Axion Dark Matter Halo Density. *The Astrophysical Journal*, **571**, 2001.

M. Baes and H. Dejonghe. Dark matter halos around elliptical galaxies: how reliable is the stellar kinematical evidence? *arXiv:astro-ph/0111137*, 2001.
URL `http://arxiv.org/abs/astro-ph/0111137`

R. Barbier, C. Brat, M. Besanon, M. Chemtob, et al. R-Parity-violating supersymmetry. *Physics Reports*, **420**:1, 2005.

M. Bartelmann and R. Narayan. Gravitational lensing and the mass distribution of clusters. *AIP Conference Proceedings*, **336**:307, 1995.

G. Battaglia, A. Helmi, H. Morrison, P. Harding, et al. The radial velocity dispersion profile of the Galactic halo: Constraining the density profile of the dark halo of the Milky Way. *Monthly Notices of the Royal Astronomical Society*, **364**:433442, 2005.

J. D. Bekenstein. The modified Newtonian dynamics - MOND and its implications for new physics. *Contemporary Physics*, **47**:387, 2006.
URL `http://www.tandfonline.com/doi/abs/10.1080/00107510701244055`

V. Belokurov, M. G. Walker, N. W. Evans, G. Gilmore, et al. Big Fish, Little Fish: Two New Ultrafaint Satellites of the Mikly Way. *The Astrophysical Journal*,

712:L103, 2010.

URL http://iopscience.iop.org/2041-8205/712/1/L103

C. L. Bennett, R. S. Hill, G. Hinshaw, M. R. Nolta, et al. FirstYear Wilkinson Microwave Anisotropy Probe (WMAP) Observations: Foreground Emission. *The Astrophysical Journal Supplement Series*, **148**:97, 2003.

URL http://iopscience.iop.org/377252

L. Bergstrom. Non-baryonic dark matter: observational evidence and detection methods. *Reports on Progress in Physics*, **63**:793, 2000.

URL http://iopscience.iop.org/0034-4885/63/5/2r3

L. Bergstrom, P. Ullio, and J. H. Buckley. Observability of rays from dark matter neutralino annihilations in the Milky Way halo. *Astroparticle Physics*, **9**:137, 1998.

URL www.sciencedirect.com/science/article/pii/S0927650598000152

G. Bertone, D. Hooper, and J. Silk. Particle dark matter: evidence, candidates and constraints. *Physics Reports*, **405**:279, 2005.

G. Bertone and D. Merritt. Dark Matter Dynamics and Indirect Detection. *Modern Physics Letters A*, **20**:1021, 2005.

R. D. Blandford and R. Narayan. Cosmological Applications of Gravitational Lensing. *Annual Review of Astronomy and Astrophysics*, **30**:311, 1992.

W. J. G. de Blok. The Core-Cusp Problem. *Advances in Astronomy*, **2010**:1, 2010.

URL http://www.hindawi.com/journals/aa/2010/789293/

W. J. G. de Blok and A. Bosma. High-resolution rotation curves of low surface brightness galaxies. *Astronomy and Astrophysics*, **385**:816, 2002.

URL http://www.edpsciences.org/10.1051/0004-6361:20020080

C. G. Bohmer and T. Harko. Can dark matter be a Bose - Einstein condensate? *Journal of Cosmology and Astroparticle Physics*, **2007**:025, 2007.
URL http://iopscience.iop.org/1475-7516/2007/06/025

C. C. Bradley, C. A. Sackett, J. J. Tollett, and R. G. Hulet. Evidence of Bose-Einstein Condensation in an Atomic Gas with Attractive Interactions. *Physical Review Letters*, **75**:1687, 1995.
URL http://link.aps.org/doi/10.1103/PhysRevLett.75.1687

W. R. Brown, M. J. Geller, S. J. Kenyon, and M. J. Kurtz. Stellar Velocity Dispersion of the Leo A Dwarf Galaxy. *The Astrophysical Journal*, **666**:231, 2007.
URL http://iopscience.iop.org/519547

A. Burkert. The structure of dark matter halos in dwarf galaxies. *The Astrophysical Journal Letters*, **447**:L25, 1995.

L. Chemin, W. J. G. De Blok, and G. A. Mamon. Improved Modeling of the Mass Distribution of Disk Galaxies by the Einasto Halo Model. *The Astronomical Journal*, **142**:109, 2011.

H. Cheng, J. L. Feng, and K. T. Matchev. Kaluza-Klein Dark Matter. *Physical Review Letters*, **89**:211301, 2002.
URL http://link.aps.org/doi/10.1103/PhysRevLett.89.211301

T.-P. Cheng. *Relativity, Gravitation and Cosmology: A Basic Introduction*. Oxford University Press, USA, 2 edition, 2010.

D. Clowe, M. Brada, A. H. Gonzalez, M. Markevitch, et al. A Direct Empirical Proof of the Existence of Dark Matter. *The Astrophysical Journal*, **648**:L109, 2006.
URL http://iopscience.iop.org/508162

M. L. M. Collins, S. C. Chapman, M. J. Irwin, N. F. Martin, et al. A Keck/DEIMOS Spectroscopic survey of the faint M31 satellites And IX, And XI, And XII and And XII. *Monthly Notices of the Royal Astronomical Society*, **407**:24112433, 2010. URL onlinelibrary.wiley.com/doi/10.1111/j.1365-2966.2010.17069.x

C. J. Copi, D. N. Schramm, and M. S. Turner. Big-Bang Nucleosynthesis and the Baryon Density of the Universe. *Science*, **267**:192, 1995. URL http://www.sciencemag.org/content/267/5195/192

K. B. Davis, M. O. Mewes, M. R. Andrews, N. J. van Druten, et al. Bose-Einstein Condensation in a Gas of Sodium Atoms. *Physical Review Letters*, **75**:3969, 1995. URL http://link.aps.org/doi/10.1103/PhysRevLett.75.3969

M. Demiaski, A. Doroshkevich, S. Pilipenko, and S. Gottlber. Simulated evolution of the dark matter large-scale structure of the Universe. *Monthly Notices of the Royal Astronomical Society*, 2011.

A. Dolgov. Neutrinos in cosmology. *Physics Reports*, **370**:333, 2002. URL www.sciencedirect.com/science/article/pii/S0370157302001394

F. Donato, G. Gentile, P. Salucci, C. Frigerio Martins, et al. A constant dark matter halo surface density in galaxies. *Monthly Notices of the Royal Astronomical Society*, **397**:1169, 2009.

J. Einasto. Dark matter. *Arxiv preprint arXiv:1109.5580*, 2011.

J. Einasto and U. Haud. Galactic models with massive corona I. - Method. *Astronomy and Astrophysics*, **223**:89, 1989.

A. Einstein. Lens-Like Action of a Star by the Deviation of Light in the Gravitational Field. *Science*, **84**:506, 1936.

J. Ellis and K. A. Olive. Supersymmetric Dark Matter Candidates. *arXiv:1001.3651*, 2010.

URL http://arxiv.org/abs/1001.3651

R. S. Ellis. Gravitational lensing: a unique probe of dark matter and dark energy. *Philosophical Transactions of the Royal Society A: Mathematical, Physical and Engineering Sciences*, **368**:967, 2010.

B. Famaey, J. Bruneton, and H. Zhao. Escaping from modified Newtonian dynamics. *Monthly Notices of the Royal Astronomical Society: Letters*, **377**:L79, 2007.

J. L. Feng. Dark Matter Candidates from Particle Physics and Methods of Detection. *Annual Review of Astronomy and Astrophysics*, **48**:495, 2010.

I. Ferrero, M. G. Abadi, J. F. Navarro, L. V. Sales, et al. The dark matter halos of dwarf galaxies: a challenge for the LCDM paradigm? *Arxiv preprint arXiv:1111.6609*, 2011.

N. Fornengo. Status and perspectives of indirect and direct dark matter searches. *Advances in Space Research*, **41**:2010, 2008.

L. Gao, J. F. Navarro, S. Cole, C. S. Frenk, et al. The redshift dependence of the structure of massive cold dark matter haloes. *Monthly Notices of the Royal Astronomical Society*, **387**:536, 2008.

URL onlinelibrary.wiley.com/doi/10.1111/j.1365-2966.2008.13277.x

K. Garrett and G. Duda. Dark Matter: A Primer. *Advances in Astronomy*, **2011**:1, 2011.

A. M. Ghez, G. Duchne, K. Matthews, S. D. Hornstein, et al. The First Measurement of Spectral Lines in a Short-Period Star Bound to the Galaxys Central Black Hole:

A Paradox of Youth. *The Astrophysical Journal*, **586**:L127, 2003.
URL http://iopscience.iop.org/374804

A. M. Ghez, S. Salim, N. N. Weinberg, J. R. Lu, et al. Measuring Distance and Properties of the Milky Ways Central Supermassive Black Hole with Stellar Orbits. *The Astrophysical Journal*, **689**:1044, 2008.
URL http://iopscience.iop.org/592738

A. Graham, D. Merritt, B. Moore, J. Diemand, et al. Empirical Models for Dark Matter Halos II. - Inner Profile Slopes and Dynamical Profiles. *The Astronomical Journal*, **132**:2701, 2006a.
URL http://iopscience.iop.org/508990

A. Graham, D. Merritt, B. Moore, J. Diemand, et al. Empirical Models for Dark Matter Halos III. - The Kormendy Relation and the log pe log Re Relation. *The Astronomical Journal*, **132**:2711, 2006b.
URL http://iopscience.iop.org/508992

A. W. Graham and S. P. Driver. A LogQuadratic Relation for Predicting Supermassive Black Hole Masses from the Host Bulge Sersic Index. *The Astrophysical Journal*, **655**:77, 2007.
URL http://iopscience.iop.org/509758

D. J. Griffiths. *Introduction to Quantum Mechanics*. Benjamin Cummings, 2nd edition, 2004.

U. Haud and J. Einasto. Galactic Models with Massive Corona II. - Galaxy. *Astronomy and Astrophysics*, **223**:95, 1989.

E. Hayashi, J. F. Navarro, C. Power, A. Jenkins, et al. The Inner Structure of Lambda-CDM Haloes II. - Halo Mass Profiles and Low Surface Brightness Galaxy Rotation Curves. *Monthly Notices of the Royal Astronomical Society*, **355**:794, 2004.

W. Hu, R. Barkana, and A. Gruzinov. Fuzzy cold dark matter: the wave properties of ultralight particles. *Physical Review Letters*, **85**:11581161, 2000.

M. Jeon, S. S. Kim, and H. B. Ann. Galactic Warps in Triaxial Halos. *The Astrophysical Journal*, **696**:1899, 2009.
URL `http://iopscience.iop.org/0004-637X/696/2/1899`

R. M. Kalas, D. Solenov, and E. Timmermans. Reentrant stability of Bose-Einstein-condensate standing-wave patterns. *Physical Review A*, **81**:053620, 2010.
URL `http://link.aps.org/doi/10.1103/PhysRevA.81.053620`

I. D. Karachentsev and Z. Xu. Optical Rotation Curves of Thin Spiral Galaxies. *Soviet Astronomy Letters*, **17**:135, 1991.
URL `http://adsabs.harvard.edu/abs/1991SvAL...17..135K`

S. Kazantzidis, B. Moore, and L. Mayer. Galaxies and Overmerging: What Does it Take to Destroy a Satellite Galaxy? *arXiv:astro-ph/0307362*, 2003.
URL `http://arxiv.org/abs/astro-ph/0307362`

J. Klaers, J. Schmitt, F. Vewinger, and M. Weitz. Bose-Einstein condensation of photons in an optical microcavity. *Nature*, **468**:545, 2010.
URL `www.nature.com/nature/journal/v468/n7323/full/nature09567.html`

A. Klypin, H. Zhao, and R. S. Somerville. Lambda-CDMbased Models for the Milky Way and M31. I. Dynamical Models. *The Astrophysical Journal*, **573**:597, 2002.
URL http://iopscience.iop.org/340656

A. Knebe and V. Wiebner. Triaxial versus Spherical Dark Matter Halo Profiles. *Pub. Astr. Soc. Australia*, **23**:125, 2006.
URL http://dx.doi.org/10.1071/AS06013

E. Komatsu, K. M. Smith, J. Dunkley, C. L. Bennett, et al. SevenYear Wilkinson Microwave Anisotropy Probe (WMAP) Observations: Cosmological Interpretation. *The Astrophysical Journal Supplement Series*, **192**:18, 2011.
URL http://iopscience.iop.org/0067-0049/192/2/18

J. Kormendy, D. B. Fisher, M. E. Cornell, and R. Bender. Structure and Formation of Elliptical and Spheroidal Galaxies. *The Astrophysical Journal Supplement Series*, **182**:216, 2009.
URL http://iopscience.iop.org/0067-0049/182/1/216

M. L. Kutner. *Astronomy: A Physical Perspective*. Cambridge University Press, 2 edition, 2003.

Y. Li and S. D. M. White. Masses for the Local Group and the Milky Way. *Monthly Notices of the Royal Astronomical Society*, **384**:1459, 2008.
URL onlinelibrary.wiley.com/doi/10.1111/j.1365-2966.2007.12748.x

M. Livio. The Dark Universe: Matter, Energy, and Gravity. *Cambridge Univ. Press, Cambridge*, 2004.

A. D. Ludlow, J. F. Navarro, S. D. M. White, M. BoylanKolchin, et al. The density and pseudophasespace density profiles of cold dark matter haloes. *Monthly Notices*

of the Royal Astronomical Society, **415**:3895, 2011.

URL onlinelibrary.wiley.com/doi/10.1111/j.1365-2966.2011.19008.x

M. Markevitch, A. H. Gonzalez, D. Clowe, A. Vikhlinin, et al. Direct Constraints on the Dark Matter SelfInteraction Cross Section from the Merging Galaxy Cluster 1E 065756. *The Astrophysical Journal*, **606**:819, 2004.

URL http://iopscience.iop.org/383178

R. Massey, J. Rhodes, R. Ellis, N. Scoville, et al. Dark matter maps reveal cosmic scaffolding. *Nature*, **445**:286, 2007.

N. J. McConnell, C.-P. Ma, K. Gebhardt, S. A. Wright, et al. Two Ten-Billion-Solar-Mass Black Holes at the Centres of Giant Elliptical Galaxies. *Nature*, **480**:215, 2011.

URL www.nature.com/nature/journal/v480/n7376/pdf/nature10636.pdf

S. S. McGaugh, M. K. Barker, and W. J. G. de Blok. A Limit on the Cosmological Mass Density and Power Spectrum from the Rotation Curves of Low Surface Brightness Galaxies. *The Astrophysical Journal*, **584**:566, 2003.

URL http://iopscience.iop.org/345806

P. J. McMillan. Mass Models of the Milky Way. *Monthly Notices of the Royal Astronomical Society*, **414**:24462457, 2011.

URL onlinelibrary.wiley.com/doi/10.1111/j.1365-2966.2011.18564.x

D. Merritt, A. Graham, B. Moore, J. Diemand, et al. Empirical Models for Dark Matter Halos. I. Nonparametric Construction of Density Profiles and Comparison with Parametric Models. *The Astronomical Journal*, **132**:2685, 2006.

URL http://iopscience.iop.org/508988

D. Merritt, J. F. Navarro, A. Ludlow, and A. Jenkins. A Universal Density Profile for Dark and Luminous Matter? *The Astrophysical Journal*, **624**:L85, 2005.
URL `http://iopscience.iop.org/430636`

E. Merzbacher. *Quantum Mechanics*. Wiley, 3 edition, 1997.

M. Milgrom. A modification of the Newtonian dynamics as a possible alternative to the hidden mass hypothesis. *The Astrophysical Journal*, **270**:365, 1983.
URL `http://adsabs.harvard.edu/doi/10.1086/161130`

M. Milgrom. MD or DM? Modified dynamics at low accelerations vs dark matter. *arXiv:1101.5122*, 2011. Proceedings of Science PoS(HRMS)033 (2010).
URL `http://arxiv.org/abs/1101.5122`

B. Moore and J. Silk. Dynamical and observable constraints on RAMBOs: Robust associations of massive baryonic objects. *The Astrophysical Journal*, **442**:L5, 1995.
URL `http://adsabs.harvard.edu/doi/10.1086/187802`

S. Nadarajah. A Generalized Normal Distribution. *Journal of Applied Statistics*, **32**:685, 2005.
URL `http://www.tandfonline.com/doi/abs/10.1080/02664760500079464`

R. Kuzio de Naray, S. S. McGaugh, W. J. G. de Blok, and A. Bosma. HighResolution Optical Velocity Fields of 11 Low Surface Brightness Galaxies. *The Astrophysical Journal Supplement Series*, **165**:461, 2006.
URL `http://iopscience.iop.org/505345`

J. F. Navarro, C. S. Frenk, and S. D. M. White. The Structure of Cold Dark Matter Halos. *The Astrophysical Journal*, **462**:563, 1996.

J. F. Navarro, E. Hayashi, C. Power, A. R. Jenkins, et al. The inner structure of Lambda-CDM Haloes III. - Universality and asymptotic slopes. *Monthly Notices of the Royal Astronomical Society*, **349**:10391051, 2004.

J. F. Navarro, A. Ludlow, V. Springel, J. Wang, et al. The diversity and similarity of simulated cold dark matter haloes. *Monthly Notices of the Royal Astronomical Society*, **402**:21, 2010.

R. K. Pathria. *Statistical Mechanics, Second Edition*. Butterworth-Heinemann, 2 edition, 1996.

L. P. Pitaevskii and S. Stringari. *Bose-Einstein Condensation*. Clarendon Press, 2004.

C. Power, J. F. Navarro, A. Jenkins, C. S. Frenk, et al. The Inner Structure of Lambda-CDM Halos I. - A Numerical Convergence Study. *Monthly Notices of the Royal Astronomical Society*, **338**:14, 2002.
URL `onlinelibrary.wiley.com/doi/10.1046/j.1365-8711.2003.05925.x`

J. I. Read, P. Saha, and A. V. Maccio. Radial Density Profiles of TimeDelay Lensing Galaxies. *The Astrophysical Journal*, **667**:645, 2007.
URL `http://iopscience.iop.org/520714`

L. J. Rosenberg and K. A. van Bibber. Searches for invisible axions. *Physics Reports*, **325**:1, 2000.

V. C. Rubin and J. Ford, W. Kent. Rotation of the Andromeda Nebula from a Spectroscopic Survey of Emission Regions. *The Astrophysical Journal*, **159**:379, 1970.

V. C. Rubin, N. Thonnard, and J. Ford, W. K. Rotational properties of 21 SC galaxies with a large range of luminosities and radii, from NGC 4605 R = 4kpc to UGC

2885 R = 122 kpc. *The Astrophysical Journal*, **238**:471, 1980.
URL http://adsabs.harvard.edu/doi/10.1086/158003

L. V. Sales, J. F. Navarro, T. Theuns, J. Schaye, et al. The origin of discs and spheroids in simulated galaxies. *Monthly Notices of the Royal Astronomical Society*, 2012.

E. Salvador-Sole, A. Manrique, and S. Serra. Origin and Modelling of Cold Dark Matter Halo Properties: I. Global Inner Structure. *Arxiv preprint arXiv:1104.2334*, 2011.

P. Schneider and A. Weiss. Light propagation in inhomogeneous universes. *The Astrophysical Journal*, **327**:526, 1988.

R. Schodel, T. Ott, R. Genzel, A. Eckart, et al. Stellar Dynamics in the Central Arcsecond of Our Galaxy. *The Astrophysical Journal*, **596**:1015, 2003.
URL http://iopscience.iop.org/378122

J. L. Sersic. Influence of the atmospheric and instrumental dispersion on the brightness distribution in a galaxy. *Boletin de la Asociacion Argentina de Astronomia La Plata Argentina*, **6**:41, 1963.
URL http://adsabs.harvard.edu/abs/1963BAAA....6...41S

P. Sikivie. Axion Cosmology. In M. Kuster, G. Raffelt, and B. Beltrn, editors, *Axions*, volume 741 of *Lecture Notes in Physics*, pp. 19–50. Springer Berlin / Heidelberg, 2008.

J. D. Simon and M. Geha. The Kinematics of the Ultrafaint Milky Way Satellites: Solving the Missing Satellite Problem. *The Astrophysical Journal*, **670**:313, 2007.
URL http://iopscience.iop.org/521816

S.-J. Sin. Late-time phase transition and the galactic halo as a Bose liquid. *Physical Review D*, **50**:3650, 1994.

M. Spano, M. Marcelin, P. Amram, C. Carignan, et al. GHASP: an H kinematic survey of spiral and irregular galaxies V. Dark matter distribution in 36 nearby spiral galaxies. *Monthly Notices of the Royal Astronomical Society*, **383**:297316, 2008.
URL `onlinelibrary.wiley.com/doi/10.1111/j.1365-2966.2007.12545.x`

D. N. Spergel, L. Verde, H. V. Peiris, E. Komatsu, et al. FirstYear Wilkinson Microwave Anisotropy Probe (WMAP) Observations: Determination of Cosmological Parameters. *The Astrophysical Journal Supplement Series*, **148**:175, 2003.
URL `http://iopscience.iop.org/377226`

S. Spivey. Astronomical Constraints on Quantum Theories of Cold Dark Matter. I. Einasto Density Profile for Galactic Halos. *submitted: Monthly Notices of the Royal Astronomical Society*, 2012.

K. Sugita, Y. Okamoto, and M. Sekine. Dark Matter Candidate Particles, CP Violation and Higgs Bosons. *International Journal of Theoretical Physics*, **47**:2875, 2008.

A. N. Taylor, D. J. Bacon, M. E. Gray, C. Wolf, et al. Mapping the 3D dark matter with weak lensing in COMBO17. *Monthly Notices of the Royal Astronomical Society*, **353**:1176, 2004.

P. Tisserand, L. Le Guillou, C. Afonso, J. N. Albert, et al. Limits on the Macho content of the Galactic Halo from the EROS-2 Survey of the Magellanic Clouds. *Astronomy and Astrophysics*, **469**:387, 2007.

W. Tucker, P. Blanco, S. Rappoport, L. David, et al. 1E 065756: A Contender for the Hottest Known Cluster of Galaxies. *The Astrophysical Journal*, **496**:L5, 1998. URL http://iopscience.iop.org/311234

M. K. Varanasi and B. Aazhang. Parametric Generalized Gaussian Density Estimation. *The Journal of the Acoustical Society of America*, **86**:1404, 1989. URL http://link.aip.org/link/?JAS/86/1404/1

J. Wang, J. F. Navarro, C. S. Frenk, S. D. M. White, et al. Assembly history and structure of galactic cold dark matter haloes. *Monthly Notices of the Royal Astronomical Society*, 2011.

A. van der Wel. The Morphology-Density Relation: A Constant of Nature. *Proceedings of the International Astronomical Union*, **3**:59, 2007.

S. D. M. White and C. S. Frenk. Galaxy formation through hierarchical clustering. *The Astrophysical Journal*, **379**:52, 1991.

R. Wojtak, S. H. Hansen, and J. Hjorth. Gravitational redshift of galaxies in clusters as predicted by general relativity. *Nature*, **477**:567, 2011.

T.-P. Woo and T. Chiueh. High-Resolution Simulation Structure Formation with Extremely Light Bosonic Dark Matter. *The Astrophysical Journal*, **697**:850, 2009. URL http://iopscience.iop.org/0004-637X/697/1/850

H. Wozniak and D. Pfenniger. The Wavy-Pattern of Stellar Rotation Curves in SBO Galaxies. volume 91, p. 445. 1996. URL http://adsabs.harvard.edu/abs/1996ASPC...91..445W

X. X. Xue, H. W. Rix, G. Zhao, P. Re Fiorentin, et al. The Milky Ways Circular Velocity Curve to 60 kpc and an Estimate of the Dark Matter Halo Mass from the

Kinematics of 2400 SDSS Blue HorizontalBranch Stars. *The Astrophysical Journal*, **684**:1143, 2008.

F. Zwicky. On the Masses of Nebulae and of Clusters of Nebulae. *The Astrophysical Journal*, **86**:217, 1937.

F. Zwicky. On the Formation of Clusters of Nebulae and the Cosmological Time Scale. *Proceedings of the National Academy of Sciences of the United States of America*, **25**:604, 1939. PMID: 16588306 PMCID: PMC1077981.

F. Zwicky. Hydrodynamics and the Morphology of Nebulae. *Physical Review*, **58**:478, 1940.

F. Zwicky. Luminous and dark formations of intergalactic matter. *Physics Today*, **6**:7, 1953.

BIOGRAPHICAL STATEMENT

Shane C. Spivey was born in 1980 in Arlington, TX. He received his B.S. and M.S. in Physics from the University of Texas at Arlington in 2006 and 2010, respectively. Shane's academic research interests include Cosmology, Particle Physics, General Relativity, Dark Matter, and Dark Energy. His technology research interests include developing sustainable energy and resource solutions for households to live off the grid, creating transportable housing, and designing open-source hardware. He currently resides in Baltimore, MD with his wife, Rani, and their border collie, Matty.